The Astrophysical Journal, 933:79 (27pp), 2022 July 1 https://doi.org/10.3847/1538-4357/ac6df1

On Atmospheric Retrievals of Exoplanets with Inhomogeneous Terminators

Luis Welbanks[1,2,3] and Nikku Madhusudhan[1]
[1] Institute of Astronomy, University of Cambridge, Madingley Road, Cambridge, CB3 0HA, UK; luis.welbanks@asu.edu
[2] School of Earth and Space Exploration, Arizona State University, Tempe, AZ 85281, USA
Received 2021 December 16; revised 2022 April 30; accepted 2022 May 3; published 2022 July 5

Abstract

The complexity of atmospheric retrieval models is largely data-driven, and one-dimensional models have generally been considered adequate with current data quality. However, recent studies have suggested that using 1D models in retrievals can result in anomalously cool terminator temperatures and biased abundance estimates even with existing transmission spectra of hot Jupiters. Motivated by these claims and upcoming high-quality transmission spectra, we systematically explore the limitations of 1D models using synthetic and current observations. We use 1D models of varying complexity, both analytic and numerical, to revisit claims of biases when interpreting transmission spectra of hot Jupiters with inhomogeneous terminator compositions. Overall, we find the reported biases to be resulting from specific model assumptions rather than intrinsic limitations of 1D atmospheric models in retrieving current observations of asymmetric terminators. Additionally, we revise atmospheric retrievals of the hot Jupiter WASP-43b ($T_{\rm eq} = 1440$ K) and the ultra-hot Jupiter WASP-103b ($T_{\rm eq} = 2484$ K), for which previous studies inferred abnormally cool atmospheric temperatures. We retrieve temperatures consistent with expectations. We note, however, that in the limit of extreme terminator inhomogeneities and high data quality, some atmospheric inferences may conceivably be biased—although to a lesser extent than previously claimed. To address such cases, we implement a 2D retrieval framework for transmission spectra that allows accurate constraints on average atmospheric properties and provides insights into the spectral ranges where the imprints of atmospheric inhomogeneities are strongest. Our study highlights the need for careful considerations of model assumptions and data quality before attributing biases in retrieved estimates to unaccounted atmospheric inhomogeneities.

Unified Astronomy Thesaurus concepts: Exoplanets (498); Exoplanet astronomy (486); Transmission spectroscopy (2133); Exoplanet atmospheres (487); Exoplanet atmospheric composition (2021)

1. Introduction

The last decade has witnessed an upsurge in transmission spectra of transiting exoplanets. Atmospheres of several dozens of exoplanets have been observed using transmission spectroscopy, i.e., observations of the wavelength-dependent change in transit depth (e.g., Seager & Sasselov 2000). Transmission spectra provide important constraints on the chemical compositions (e.g., Charbonneau et al. 2002; Deming et al. 2013; Sing et al. 2016), presence of clouds and hazes (e.g., Pont et al. 2008; Lecavelier Des Etangs et al. 2008a, 2008b; Kreidberg et al. 2014a; Benneke et al. 2019), and other atmospheric properties at the day–night terminator regions of exoplanets (see, e.g., Madhusudhan 2019, for a review).

Concurrent with this data flood, atmospheric models of varying degrees of complexity have been developed to provide theoretical expectations for the observations and aid in their interpretation. These models range from relatively simple one-dimensional (1D) atmospheres (e.g., Seager & Sasselov 1998; Brown 2001; de Wit & Seager 2013; Goyal et al. 2018) to more complex three-dimensional (3D) general circulation models (GCM; e.g., Showman et al. 2009; Parmentier et al. 2016). Independent of their dimensionality, atmospheric models have a series of physical processes and assumptions built into them to make their computation achievable and apt for their intended purpose. Such assumptions can range from considering isothermal and isobaric atmospheres (e.g., Heng & Kitzmann 2017) and determining chemical abundances following chemical equilibrium expectations (e.g., Goyal et al. 2018), to considering clouds, dynamics, and disequilibrium chemistry (e.g., Moses et al. 2011; Venot et al. 2012; Moses et al. 2013; Parmentier et al. 2016; Venot et al. 2020; Steinrueck et al. 2021).

The investigation of multidimensional effects in transmission spectra dates back to first detection of an atmosphere around a transiting exoplanet (Brown et al. 2001; Charbonneau et al. 2002). In order to investigate the apparent disparity between the predicted and observed strength of the Na absorption feature in the hot Jupiter HD 209458b, Fortney et al. (2003) modeled the transmission spectrum for a two-dimensional (2D) atmosphere, considering the angular dependence of Na ionization across the day and night sides of the planet. Several subsequent studies have considered multidimensional (2D/3D) models of transmission spectra with varying degrees of sophistication and functionality (e.g., Iro et al. 2005; Burrows et al. 2010; Fortney et al. 2010).

When interpreting observations, the complexity of the models employed is largely driven by the quality of the data. If the precision and/or resolution of the data are not sufficient to distinguish the impact of a computationally expensive consideration, this overly complex calculation may not be warranted for the purposes of inferring atmospheric properties from spectra. This is particularly the case for atmospheric retrievals of exoplanets, which compute 10^5–10^6 atmospheric models spanning a wide range of physical conditions and parameter space to obtain statistical constraints on the atmospheric properties of an exoplanet from an observed spectrum

[3] NHFP Sagan Fellow.

(see, e.g., Madhusudhan 2018, for a recent review). Therefore, retrieval frameworks have generally been limited to 1D parametric models with certain assumptions intended to ease their computational efficiency.

Naturally, a key question arises: What are the key physical processes and model assumptions permitted by the data in order to obtain robust and reliable atmospheric inferences using atmospheric retrievals? Answering this question is paramount, given recent observational advancements enabling high-precision transmission spectra of exoplanets over a broad spectral range (e.g., Deming et al. 2013; Kreidberg et al. 2014b; Sing et al. 2016; Nikolov et al. 2018). Additionally, the launch of the James Webb Space Telescope (JWST) and the promise of spectroscopic data over a wide wavelength range with unprecedented precision (e.g., Greene et al. 2016) may mean that previously unwarranted model considerations will now be needed. Indeed, a flourishing area of research has emerged around the investigation of possible limitations of 1D retrieval models, especially within the context of planets with cloud inhomogeneities as well as thermal and chemical inhomogeneities (e.g., Line & Parmentier 2016; Caldas et al. 2019; Pluriel et al. 2020; Lacy & Burrows 2020; MacDonald et al. 2020; Espinoza & Jones 2021; Pluriel et al. 2022).

Line & Parmentier (2016) explored the effect of inhomogeneous clouds on atmospheric retrievals of transmission spectra. Their study suggests that changes in spectral shape, i.e., the wavelength-dependent slope of the transit depth, due to the presence of inhomogeneous clouds can be modeled as the linear combination of a cloudy and a non-cloudy model. This modeling approach has been expanded to combined effects of inhomogeneous clouds and hazes in exoplanet atmospheres (e.g., MacDonald & Madhusudhan 2017; Welbanks & Madhusudhan 2021) and inhomogeneities in the temperature structure and chemical composition between terminators (e.g., MacDonald et al. 2020; Espinoza & Jones 2021). Similar treatments of inhomogeneities have also been applied to thermal emission spectra (e.g., Feng et al. 2016; Taylor et al. 2020; Feng et al. 2020) and to the effects of stellar heterogeneities on transmission spectra (e.g., Pinhas et al. 2018; Iyer & Line 2020) of exoplanets.

Other recent studies have investigated the impact of nonuniform day and night sides with thermal and chemical inhomogeneities on retrievals using 1D atmospheric models (e.g., Caldas et al. 2019; Pluriel et al. 2020; Lacy & Burrows 2020; Pluriel et al. 2022). Caldas et al. (2019) develop a 3D radiative transfer model, create synthetic JWST observations for a planet with day–night temperature inhomogeneities, and retrieve the properties of the synthetic observations using cloud-free isothermal 1D atmospheric models. Their results suggest that, while 1D models can provide a good match to the data, the retrieved atmospheric properties may be biased. In particular, for planets with large thermal gradients between the day and night sides, such as ultra-hot Jupiters, the retrieved temperature for transmission spectra may be higher than the terminator temperature when using 1D, cloud-free, isothermal models. Similar conclusions were reached by Pluriel et al. (2020), who find that 1D isothermal models with homogeneous clouds may retrieve biased molecular abundances if confronted with synthetic JWST observations of planets with day–night chemical heterogeneities.

Lacy & Burrows (2020) further explore the impact of day–night temperature gradients on atmospheric retrievals. They propose a parameterization to recover the pressure–temperature (P–T) profile of an atmosphere with day–night temperature gradients, and investigate the combined effects of day–night temperature gradients and aerosols. Their results, based on synthetic JWST-like observations and assumptions of chemical equilibrium, suggest that day–night temperature gradients may be detectable in the future. Similarly, Pluriel et al. (2022) find that assuming isothermal P–T profiles can lead to biased results when interpreting observations of planets with day–night inhomogeneities. Their results, based on cloud-free models, suggest that JWST-like data will require accounting for non-isothermal temperature structures, as normally done in retrievals (e.g., Madhusudhan & Seager 2009).

Besides day–night inhomogeneities, exoplanets may also have nonuniform morning and evening terminators. In order to constrain the properties of these morning and evening terminators, Espinoza & Jones (2021) present a framework to produce distinct transmission spectra for each planetary limb. Additionally, they modify the retrieval framework CHIMERA (Line et al. 2013) to compute chemically consistent retrievals (i.e., assuming chemical equilibrium) using the linear combination of two 1D atmospheric models, each for a planet limb, as initially proposed by Line & Parmentier (2016). Using real Hubble Space Telescope (HST) data and synthetic JWST data, their results suggest that obtaining separate transmission spectra for each planetary limb and performing a retrieval on them may be a fruitful approach to constrain the atmospheric properties of inhomogeneous planets.

Recent studies have also claimed anomalous retrieved atmospheric temperatures in hot Jupiters with existing observations of transmission spectra. A study by MacDonald et al. (2020), hereafter MGL20, investigated the impact of morning and evening terminator inhomogeneities. Their work claims to find an important anomaly in retrievals of transiting exoplanets using existing observations: the retrieved atmospheric temperatures are notably cooler than expectations from the equilibrium temperature of the planet. They investigate the origin of this bias using analytic derivations and retrieving synthetic HST observations using 1D models. Using cloud-free models, they find that the retrieved abundances and temperature profiles for observations of present-day quality can be significantly biased as a result of asymmetric terminators. They conclude that chemical abundances from 1D retrieval techniques are often biased. Such thermal anomalies are also reported by other recent studies performing atmospheric retrievals on ground- and space-based transmission spectra (e.g., Weaver et al. 2020; Kirk et al. 2021). Our present work investigates these anomalies further.

These studies raise compelling concerns regarding the reliability and robustness of 1D atmospheric models. In particular, the inferred anomalies in the retrieved atmospheric temperatures could mean that 1D retrieval techniques are often biased in their retrieved chemical abundances and associated efforts to constrain planet formation mechanisms from atmospheric abundances. Therefore, there is an urgent need to understand the origin and influence of these thermal biases under different planetary conditions. Moreover, it is imperative to establish whether conclusions derived using isothermal models can be generalized to results from non-isothermal models. Likewise, it is important to ascertain whether the lessons derived from cloud-free models are applicable to models considering the presence of inhomogeneous clouds and

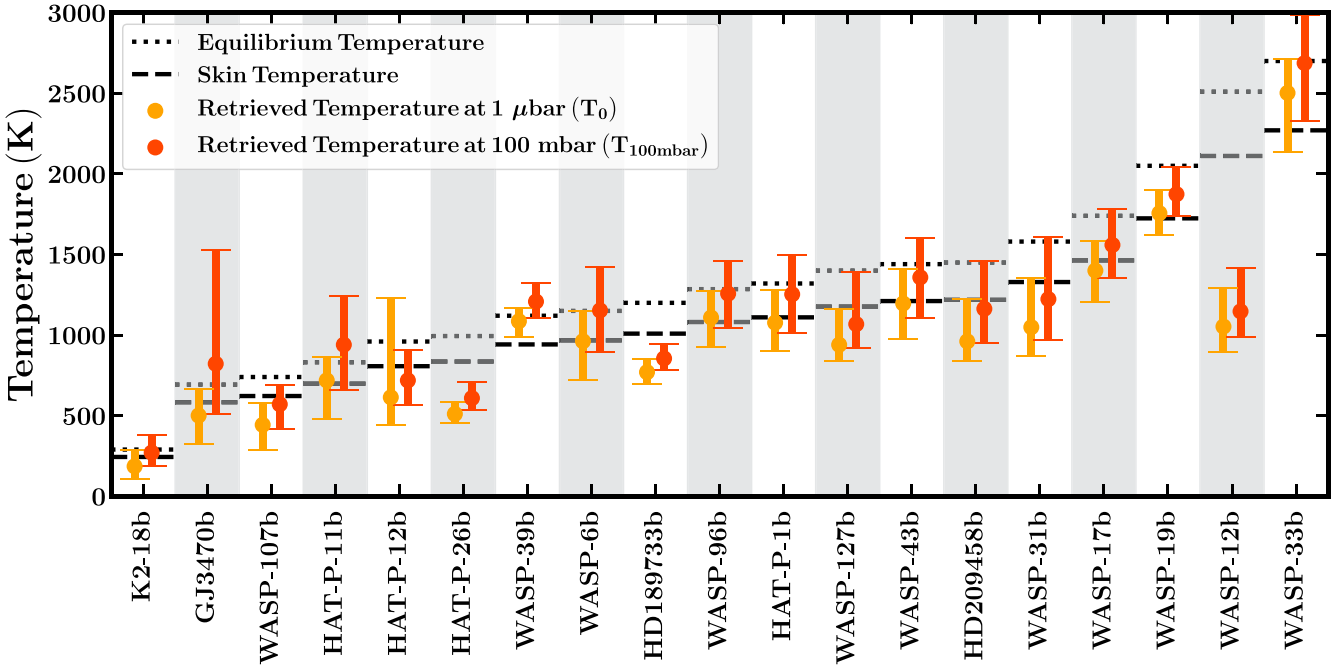

Figure 1. Equilibrium temperatures (T_{eq}, dotted line) and skin temperatures ($T_{skin} = 2^{-1/4}\,T_{eq}$, dashed line) for the planets in the sample of Welbanks et al. (2019). Retrieved temperatures (T_{ret}) at different pressures and their 1σ confidence intervals are shown in yellow (1 μbar, T_0) and orange (100 mbar, $T_{100mbar}$). Also see Table 1.

hazes. Finally, the reliability of state-of-the-art retrieval frameworks with more flexible 1D models considering non-isothermal temperature profiles, inhomogeneous clouds and hazes, and multiple sources of opacity needs to be established.

In the present paper, we investigate the reliability of atmospheric temperature estimates from 1D atmospheric models. In particular, we address claims of seemingly anomalous temperatures from retrievals of hot Jupiters from MGL20. Additionally, we implement a two-dimensional (2D) chemically unconstrained retrieval approach for exoplanetary transmission spectra. In Section 2, we revisit published retrieval studies of transmission spectra for a wide sample of exoplanets spanning cool mini-Neptunes to ultra-hot Jupiters, and assess whether their retrieved atmospheric temperatures match expectations derived from their equilibrium temperatures and GCM studies. Then, in Section 3, we investigate the impact of asymmetric morning evening terminators on the retrieved atmospheric temperatures using semi-analytic models and retrievals.

Next, in Section 4, we perform a systematic exploration of retrieved temperature estimates over a wide range of planetary conditions ranging from warm to ultra-hot Jupiters using different families of 1D atmospheric models. We investigate the impact of asymmetric terminators on 1D atmospheric models and their inferred atmospheric properties. We expand our investigation in Section 5 by performing retrievals on existing observations of hot/ultra-hot Jupiters for which previous studies (e.g., Weaver et al. 2020; Kirk et al. 2021) inferred anomalously cool atmospheric temperatures. We investigate whether these retrieved thermal biases are the result of simplified model considerations or anomalies in 1D models due to asymmetric terminators.

Subsequently, in Section 6, we introduce a 2D atmospheric model in a "free-retrieval" framework to retrieve the atmospheric properties of planets with asymmetric terminators. A similar approach has been implemented recently by Espinoza & Jones (2021), with constraints of chemical equilibrium. This new multidimensional approach retrieves the atmospheric properties of planets with inhomogeneous terminators. Additionally, this framework provides important information about the wavelength ranges most affected by these inhomogeneities, as well as the chemical species with non-homogeneous abundances. We summarize our results and key lessons in Section 7, where we also discuss the prospects for future investigations of multidimensional effects in exoplanetary transmission spectra.

2. On Retrieved Temperature Anomalies from the Literature

With the growing number of transmission spectra for exoplanet atmospheres, recent studies have pursued systematic explorations of these observations using retrieval frameworks to address population level hypothesis about planet composition and formation (e.g., Madhusudhan et al. 2014; Barstow et al. 2017; Pinhas et al. 2019; Welbanks et al. 2019). A byproduct of such studies is a large sample of planetary spectra analyzed under similar model assumptions and for which the inferred atmospheric properties can be compared among planets in the sample. One such study (Welbanks et al. 2019) was used as a reference by MGL20 to postulate an anomaly in retrieval studies of transmission spectra. Specifically, MGL20 state that almost all retrieved temperatures are notably cooler than the planetary equilibrium temperature. Here, we seek to investigate the origin of these anomalies. We revisit the inferred atmospheric properties from the complete sample of 19 planets from Welbanks et al. (2019) and compare their retrieved temperatures (T_{ret}) to the calculated equilibrium (T_{eq}) and skin (T_{skin}) temperatures of the planet. We summarize the retrieved atmospheric temperatures from Welbanks et al. (2019) in Figure 1 and Table 1.

The atmospheric models in Welbanks et al. (2019) use non-isothermal P–T profiles. As a result, the temperature in the

Table 1
Retrieved Temperatures from Exoplanet Transmission Spectra

Planet	T_{eq} (K)	T_{skin} (K)	T_{ret} (K)	$T_{ret} - T_{eq}$ (K)	$\frac{T_{ret}}{T_{skin}}$	…	Planet	T_{eq} (K)	T_{skin} (K)	T_{ret} (K)	$T_{ret} - T_{eq}$ (K)	$\frac{T_{ret}}{T_{skin}}$
K2-18b	290	244	271^{+112}_{-80}	-19^{+112}_{-80}	$1.11^{+0.46}_{-0.33}$		HAT-P-1b	1320	1110	1253^{+246}_{-243}	-67^{+246}_{-243}	$1.13^{+0.22}_{-0.22}$
GJ 3470b	693	583	822^{+705}_{-313}	129^{+705}_{-313}	$1.41^{+1.21}_{-0.54}$		WASP-127b	1400	1177	1068^{+323}_{-145}	-332^{+323}_{-145}	$0.91^{+0.27}_{-0.12}$
WASP-107b	740	622	571^{+122}_{-156}	-169^{+122}_{-156}	$0.92^{+0.20}_{-0.25}$		WASP-43b	1440	1211	1358^{+247}_{-252}	-82^{+247}_{-252}	$1.12^{+0.20}_{-0.21}$
HAT-P-11b	831	699	940^{+300}_{-280}	109^{+300}_{-280}	$1.34^{+0.43}_{-0.40}$		HD 209458b	1450	1219	1163^{+299}_{-210}	-287^{+299}_{-210}	$0.95^{+0.25}_{-0.17}$
HAT-P-12b	960	807	719^{+189}_{-154}	-241^{+189}_{-154}	$0.89^{+0.23}_{-0.19}$		WASP-31b	1580	1329	1223^{+386}_{-251}	-357^{+386}_{-251}	$0.92^{+0.29}_{-0.19}$
HAT-P-26b	994	836	609^{+102}_{-72}	-385^{+102}_{-72}	$0.73^{+0.12}_{-0.09}$		WASP-17b	1740	1463	1559^{+221}_{-204}	-181^{+221}_{-204}	$1.07^{+0.15}_{-0.14}$
WASP-39b	1120	942	1208^{+115}_{-101}	88^{+115}_{-101}	$1.28^{+0.12}_{-0.11}$		WASP-19b	2050	1724	1874^{+167}_{-135}	-176^{+167}_{-135}	$1.09^{+0.10}_{-0.08}$
WASP-6b	1150	967	1153^{+268}_{-259}	3^{+268}_{-259}	$1.19^{+0.28}_{-0.27}$		WASP-12b	2510	2111	1147^{+268}_{-161}	-1363^{+268}_{-161}	$0.54^{+0.13}_{-0.08}$
HD 189733b	1200	1009	855^{+88}_{-70}	-345^{+88}_{-70}	$0.85^{+0.09}_{-0.07}$		WASP-33b	2700	2270	2687^{+301}_{-362}	-13^{+301}_{-362}	$1.18^{+0.13}_{-0.16}$
WASP-96b	1285	1081	1257^{+202}_{-211}	-28^{+202}_{-211}	$1.16^{+0.19}_{-0.20}$							

Notes. Equilibrium temperatures $\left(T_{eq} = \left[f(1 - A_B)\left(\frac{R_{star}}{2a}\right)^2\right]^{\frac{1}{4}} T_{eff.,star}\right)$ assuming no bond albedo ($A_B = 0$) and full energy redistribution ($f = 1$) from Welbanks et al. (2019) and reported in MacDonald et al. (2020). The skin temperature is given by $T_{skin} = 2^{-1/4}\, T_{eq}$. Here, T_{ret} is the retrieved temperature at a pressure of 100 mbar, close to the slant photosphere, from Welbanks et al. (2019).

atmosphere varies vertically. Due to the lack of thermal inversions in the retrieved *P–T* profiles, the temperature at the top atmosphere will generally be cooler than the temperatures deeper in the atmosphere. Figure 1 shows the temperature estimates at the top of the model atmosphere (T_0) at a pressure of 10^{-6} bar (in yellow), and the temperature estimates near the photosphere ($T_{100mbar}$) at a pressure of 100 mbar (in orange). The temperature estimates near the photosphere are warmer than the temperature estimates at the top of the atmosphere. This difference in temperature estimates was not considered by MGL20, who used the cooler temperature estimates at the top of the atmosphere instead of the more representative and warmer retrieved temperature near the photosphere.

Furthermore, when reporting the estimated difference between T_{ret} and T_{eq} or T_{skin}, MGL20 restricted their comparison to the median values only, without considering the uncertainties in the retrieved parameters. Figure 1 and Table 1 include the inferred 1σ confidence intervals for the estimated temperatures (i.e., the "error" in the estimate). For most planets, T_{ret} and T_{eq} are consistent within 1σ. Additionally, the ratio between T_{ret} and T_{skin} is consistent with unity for most planets. As such, there is no anomaly in the retrieved temperatures for most planets in the sample.

Three planets have retrieved temperatures near the photosphere that are inconsistent with their T_{eq} and T_{skin}. HAT-P-26b and HD 189733b have inconsistencies of $\lesssim$300 K. Considering that T_{eq} may not be representative of the temperature at the terminator, and given the assumption of full redistribution and zero albedo in the computation of the values presented in Table 1, this apparent discrepancy may be not significant. Finally, WASP-12b has an inconsistency of $\gtrsim$1000 K. This outlier would warrant a detailed inspection of the data and model considerations employed to better understand the origin of this anomaly, as discussed below. Overall, when considering the entire sample, a comparison of the median retrieved temperatures at the photosphere with the skin temperature shows no consistent trend of underestimated temperatures.

It is also important to consider that the photospheric temperature at the terminator of the planet can be lower than T_{eq} and T_{skin}. As mentioned above, the calculation of T_{eq} requires making some assumptions about the energy redistribution between the day and night sides of the planet, as well as the planetary albedo. Therefore, assuming different values for the planetary albedo or energy redistribution can result in cooler estimates. For instance, assuming a bond albedo of 0.1, the equilibrium temperatures reported in Table 1 would decrease by ∼20 K for the warm mini-Neptunes and up to ∼70 K for the ultra-hot Jupiters.

On the other hand, $T_{skin} = 2^{-1/4}\, T_{eq}$ is the temperature estimate of a hypothetical outer atmospheric layer with low optical depth, transparent to incident stellar radiation and heated only by outgoing radiation, for a gray atmosphere (Pierrehumbert 2010; Parmentier & Guillot 2014). This temperature estimate would not necessarily represent the photospheric temperature at the terminator. Furthermore, Parmentier & Guillot (2014) show that non-gray effects can lead to skin temperatures significantly lower than those predicted for the gray case. Although MGL20 argue for T_{eq} and T_{skin} as the reference values for the terminator temperature expectations, in practice any temperature estimate would be better gauged by GCMs, which are expected to provide more realistic estimates of these values (Seager 2010). Therefore, we inform our expectations using GCM results from the literature below.

GCMs show that the atmospheric temperature of the planet is dependent on a series of factors, including the atmospheric composition and the orbital phase of the planet. For instance, for the hot Neptune GJ436b, Lewis et al. (2010) find zonal-mean temperatures at 10 mbar of $T_{10\ mbar} \sim 500$–550 K for a $1\times$ solar composition, estimates cooler than T_{eq} and T_{skin} ($T_{eq} = 649$ K, $T_{skin} = 546$ K). Similarly, for the high-eccentricity hot Jupiter HAT-P-2b, Lewis et al. (2014) find temperature averages over latitude and longitude of $T \lesssim 1200$ K at P $\sim 10^{-3}$–10^{-1} bar at the time of transit, estimates lower than T_{eq} and T_{skin} ($T_{eq} = 1481$ K, $T_{skin} = 1246$ K).

More recently, Kataria et al. (2016) have modeled nine hot Jupiters common to the sample in Welbanks et al. (2019). Their study models HAT-P-12b, WASP-39b, WASP-6b, HD 189733b, HAT-P-1b, HD 209458b, WASP-31b, WASP-17b, and WASP-19b, with reported values of T_{eq} close to those in Table 1. Their results show that the temperature probed in transmission can be significantly cooler than the T_{eq} and T_{skin} of the planet. For instance, the pressures probed in transmission

for the hot Jupiter WASP-19b ($T_{eq} \sim 2050$ K, $T_{skin} \sim 1724$ K) can correspond to temperatures as cool as $\lesssim$1400 K cooler than T_{skin} and T_{eq}. Similarly, a cooler planet like WASP-39b ($T_{eq} = 1120$ K, $T_{skin} = 942$ K) exhibits temperatures cooler than T_{skin} and T_{eq} probed in transmission, with values as low as $\lesssim$900 K. Similar results are shown for the ultra-hot Jupiter WASP-12b ($T_{eq} \sim 2510$ K, $T_{skin} \sim 2111$ K) in a recent study by Arcangeli et al. (2021), where the brightness temperatures at the terminator near photospheric pressures, $T_{1\ mbar} \sim 1000$–2000 K, can be cooler than T_{eq} and T_{skin}.

Considering these estimates from the literature, most temperature estimates from Welbanks et al. (2019) shown in Figure 1 and Table 1 are well within the physically plausible range for the photospheric temperature of the terminator. Overall, depending on the atmospheric composition and the pressures probed by the photosphere, the temperature at the terminator of the planet can be significantly cooler than the T_{eq} and T_{skin} of the planet. Future studies may investigate how these considerations affect the photospheric temperature near the terminator of the planet, to better inform our expectations for ultra-hot Jupiters.

Notwithstanding the fact that we do not find anomalous retrieved temperature estimates in the published results of Welbanks et al. (2019), we investigate other claims made in previous studies. For example, MGL20 claim an analytic justification for substantially cooler temperature estimates. From this analytic solution, they state that compositional biases exceeding a factor of two result in temperature biases of hundreds of degrees. Additionally, they state that no equivalent temperature can reproduce a 2D spectrum using a 1D model. MGL20 claim that these thermal biases hold for state-of-the-art retrieval codes and that the chemical abundances derived from 1D retrieval techniques are often biased. Finally, they claim to confirm these biases using atmospheric retrievals with synthetic data. Other studies have also reported seemingly anomalous temperature estimates with observed transmission spectra of several hot/ultra-hot Jupiters (e.g., Weaver et al. 2020; Kirk et al. 2021). We explore these claims systematically in the sections below.

In Section 3 and in Appendix A, we demonstrate analytically that the inferred temperatures from 1D models are the averages of the morning and evening terminators. In Section 3.2, we verify our expectations using semi-analytic retrievals and show that 1D models can reproduce 2D spectra. In Section 4, we use the same atmospheric cases as MGL20 and state-of-the-art retrievals with established P–T parameterizations and generalized cloud and haze prescriptions to investigate the claimed thermal biases. Using the same atmospheric models, in Section 5 we reanalyze observations from Weaver et al. (2020) and Kirk et al. (2021) to investigate their seemingly anomalous temperature inferences. Finally, in 7.1 we discuss how several of the simulated retrieval estimates in MGL20 indeed seem consistent with the true temperature and abundance values, if the statistical uncertainties are considered.

3. Exploring Semi-analytic Solutions for Asymmetric Terminators

Analytic treatments of the transit depth of exoplanets (e.g., Brown 2001; Lecavelier Des Etangs et al. 2008a; Bétrémieux & Swain 2017; Heng & Kitzmann 2017) can be useful to understand the origin of a planetary spectrum and its dependence on physical parameters such as temperature and chemical composition. However, the analytical tractability of such expressions is based on assumptions of isobaric cross sections in isothermal atmospheres with assumptions of constant gravity and scale heights (e.g., Heng & Kitzmann 2017). These unphysical assumptions can lead to biased atmospheric interpretations when compared to more physically plausible numerical models (Welbanks & Madhusudhan 2019). Nonetheless, these analytic treatments are routinely used to provide a theoretical basis for our understanding of exoplanet atmospheres.

Indeed, MGL20 follow such a semi-analytic approach to construct a theoretical justification for their inferred biased temperatures. They derive an equivalent 1D temperature for a 2D atmosphere with asymmetric terminators. Here, we seek to investigate the expectations for this equivalent 1D temperature using the same semi-analytic approach.

3.1. Analytic Temperature and Abundance Expectations

First, we begin with the general wavelength-dependent transit depth

$$\Delta_\lambda = \frac{\pi R_p^2 + \int_0^{2\pi}\int_{R_p}^{\infty}(1 - e^{-\tau_\lambda(b,\theta)})\, b\, db\, d\theta}{\pi R_{star}^2}, \quad (1)$$

where R_p and R_{star} are the planetary radius and stellar radius, respectively, b is the impact parameter, τ_λ is the slant optical depth, and θ is the azimuthal angle. We can split the contribution of the optical depth in Equation (1) into two separate integrals, as proposed by MGL20, each representing half of a planetary hemisphere, a morning one and an evening one, as

$$\Delta_{\lambda,2D} = \frac{R_p^2 + \int_{R_p}^{\infty} b(1 - e^{-\tau_{\lambda,M}(b)})db + \int_{R_p}^{\infty} b(1 - e^{-\tau_{\lambda,E}(b)})db}{R_{star}^2}. \quad (2)$$

This result is equivalent to taking the well-known expression for 1D atmospheres in transmission geometry (e.g., MacDonald & Madhusudhan 2017; Welbanks & Madhusudhan 2021) and reformulating the contribution of the atmosphere as a linear combination of two distinct 1D atmospheres, one for the evening "E" and the other for the morning "M."

Then, in order to easily evaluate the integrals of the above expressions, one can assume isobaric and isothermal conditions, a single chemical absorber, and constant gravity and scale height ($H = kT/\mu g$), as previously done in numerous works (e.g., Lecavelier Des Etangs et al. 2008a; de Wit & Seager 2013; Bétrémieux & Swain 2017; Heng & Kitzmann 2017; Sing 2018). With the above assumptions, considering two separate semi-hemispheres (morning and evening) with distinct isothermal temperatures and associated scale heights ($H_E = kT_E/\mu g$ for the evening and $H_M = kT_M/\mu g$ for the morning), Equation (2) simplifies to

$$\Delta_{\lambda,2D} = \frac{R_p^2 + R_p H_M(\gamma + \ln\tau_{0,\lambda,M}) + R_p H_E(\gamma + \ln\tau_{0,\lambda,E})}{R_{star}^2}, \quad (3)$$

with $\tau_{0,\lambda,i}$ given under the assumption of isobaric cross sections and hydrostatic equilibrium as

$$\tau_{0,\lambda,i} = \frac{P_0}{kT_i}\sqrt{2\pi R_p H_i} X \sigma_\lambda, \quad (4)$$

where the index i is used to represent the evening (E) or morning (M) parameters, and X and σ are the single chemical absorber's volume mixing ratio and cross section. Similarly, the 1D semi-analytic transmission spectrum is

$$\Delta_{\lambda,1D} = \frac{R_p^2 + 2R_p H_{1D}(\gamma + \ln \tau_{0,\lambda,1D})}{R_{star}^2}, \quad (5)$$

with only one isothermal temperature T_{1D}, its associated scale height $H_{1D} = kT_{1D}/\mu g$, and $\tau_{0,\lambda,1D}$ given by Equation (4) with the 1D temperature, scale height, and abundances.

MGL20 investigate the resulting atmospheric properties from using a 1D model to interpret the transmission spectrum of a 2D model atmosphere, using the semi-analytic expressions in Equations (3) and (5). They investigate the isothermal temperature of an equivalent 1D model to produce the same transit depth as a 2D model at a given wavelength, i.e., $\Delta_{\lambda,2D} = \Delta_{\lambda,1D}$. According to MGL20, while one may expect the 1D model to obtain an average temperature (i.e., $T_{1D} = \bar{T} = \frac{1}{2}(T_E + T_M)$) they find T_{1D} to be lower than $\bar{T}$. This result was used by MGL20 to explain the erroneously cold temperatures presumably derived using 1D retrievals of hot Jupiters, with further implications for retrieved abundance estimates.

We revisit the analytic formulation in Appendix A to assess this result. MGL20 equate the transit depths of the 1D and 2D models at a single wavelength, implicitly assuming that the atmospheric properties can be inferred from a single transit depth measurement, which is not feasible. In practice, it is the shape of a transmission spectrum, i.e., the gradient of the transit depth with wavelength, that provides constraints on the atmospheric properties in transmission geometry (Lecavelier Des Etangs et al. 2008a; Benneke & Seager 2012; Line & Parmentier 2016; Sing 2018). Therefore, we equate the spectral shapes between the 1D and 2D models in order to determine the relation between the 1D and 2D atmospheric properties.

In contrast to MGL20, as shown in Appendix A, we find that an equivalent 1D model can indeed recover the 1D temperature as the average of the morning and evening temperatures in the 2D model, i.e., $T_{1D} = \bar{T}$. Our analysis also recovers the well-known degeneracy due to the unphysical assumptions of this semi-analytic formalism between the chemical abundances and the reference pressure of the planet (see, e.g., Lecavelier Des Etangs et al. 2008a; Heng & Kitzmann 2017; Welbanks & Madhusudhan 2019). Furthermore, the atmospheric properties of the 1D model as a function of the properties of the 2D model are related as

$$P_{0,1D}\, X_{1D}\, \sigma_{\bar{T}} = \bar{T}^{\frac{1}{2}} (P_{0,M}\, X_M\, \sigma_M)^{\frac{\beta}{2}} (P_{0,E}\, X_E\, \sigma_E)^{\frac{\alpha}{2}} \times (\bar{T} - \Delta T)^{-\frac{\beta}{4}} (\bar{T} + \Delta T)^{-\frac{\alpha}{4}}. \quad (6)$$

Here, for each morning (M), evening (E), or 1D model (1D): X_i is the chemical abundance, σ_i is the temperature-dependent cross section, $P_{0\,i}$ is the reference pressure, $\alpha = 1 + \frac{\Delta T}{\bar{T}}$, $\beta = 1 - \frac{\Delta T}{\bar{T}}$, $\bar{T} = \frac{T_E + T_M}{2}$, and $\Delta T = \frac{T_E - T_M}{2}$.

In order to derive a 1D chemical abundance in this analytic framework, one must assume a reference pressure, or vice versa (e.g., Lecavelier Des Etangs et al. 2008a). Additionally, Equation (6) shows that the 1D chemical abundance is not expected to be the average of the morning and evening abundances as assumed by MGL20. We test the predictions from our derivation using an atmospheric retrieval framework below.

3.2. Atmospheric Retrieval Using Semi-analytic Models

We generate a synthetic HST-WFC3 transmission spectrum following the 2D semi-analytic atmospheric model in Equation (3), and then retrieve the atmospheric properties using the 1D semi-analytic model in Equation (5). The system properties in the atmospheric model employed to generate the synthetic observations and in the atmospheric retrieval are those of the canonical hot Jupiter HD 209458b: $R_p = 1.359 R_J$ with $R_{p,ref} = 1.33182\, R_J$ as the assumed reference radius following MGL20, $M_p = 0.685\, M_J$, and $R_{star} = 1.155\, R_\odot$ (Torres et al. 2008). To satisfy the assumptions of the semi-analytic treatments, we employ isothermal atmospheres with a single absorber, H_2O. The assumption of isobaric cross sections from this semi-analytic treatment is satisfied by calculating the H_2O cross sections at 10 bar. The mean molecular weight is fixed to 2.3 amu.

Similarly to Section 2.1 of Welbanks & Madhusudhan (2019), we replace the numerical atmospheric model in the retrieval framework of Welbanks & Madhusudhan (2021) with the semi-analytic model in Equation (5). The parameter estimation is performed using the nested sampling algorithm MultiNest (Feroz et al. 2009, 2019) through the implementation PyMultiNest (Buchner et al. 2014). The priors used are explained in Appendix B. The synthetic observations follow the resolution ($R = 60$) and precision (50 ppm) chosen by MGL20 for HST-WFC3, representative of current HST observations (e.g., Sing et al. 2016). The model spectra are generated by sampling the high-resolution opacities at their native resolution (0.1 cm^{-1}). The high-resolution models are binned to the instrumental resolution to perform the model–data comparison (see, e.g., Pinhas et al. 2019, and Section 4.1). The synthetic data do not include Gaussian scatter, following the approach of MGL20.

The 2D semi-analytic model that produced the synthetic observations assumes a warm evening terminator with an isothermal temperature $T_E = 2000$ K, H_2O volume mixing ratio of $\log_{10}(X_{H_2O})_E = -6.0$, and a reference pressure of 10 bar. The cooler morning terminator assumes an isothermal temperature $T_M = 1000$ K and $\log_{10}(X_{H_2O})_M = -3.0$. The reference pressure for the morning terminator is derived in Appendix A.1 to be ~7 mbar, assuming that the reference radius in the deep atmosphere is the same between the morning and evening terminator and that both reference points correspond to the same optical depth surface. The chosen input values are only illustrative, and have been selected to represent an extreme case of thermal and chemical inhomogeneities.

Using the above input values, the expected retrieved isothermal temperature for the 1D model would be $T_{1D} = \frac{1}{2}(T_E + T_M) = \frac{1}{2}(2000 + 1000) = 1500$ K. As dictated by Equation (6), without any assumptions about the reference pressure of the 1D model, we expect a degeneracy between the chemical abundance and reference pressure. First, we perform a retrieval for which we retrieve the 1D isothermal temperature, 1D H_2O mixing ratio, and 1D reference pressure for a radius of $R_{p,ref} = 1.33182 R_J$. Figures 2 and 3 show the results from this retrieval.

In agreement with the expectations from our semi-analytic derivation, our retrieval finds a 1D isothermal temperature of $T_{1D} = 1487^{+72}_{-73}$ consistent with the average of the input morning

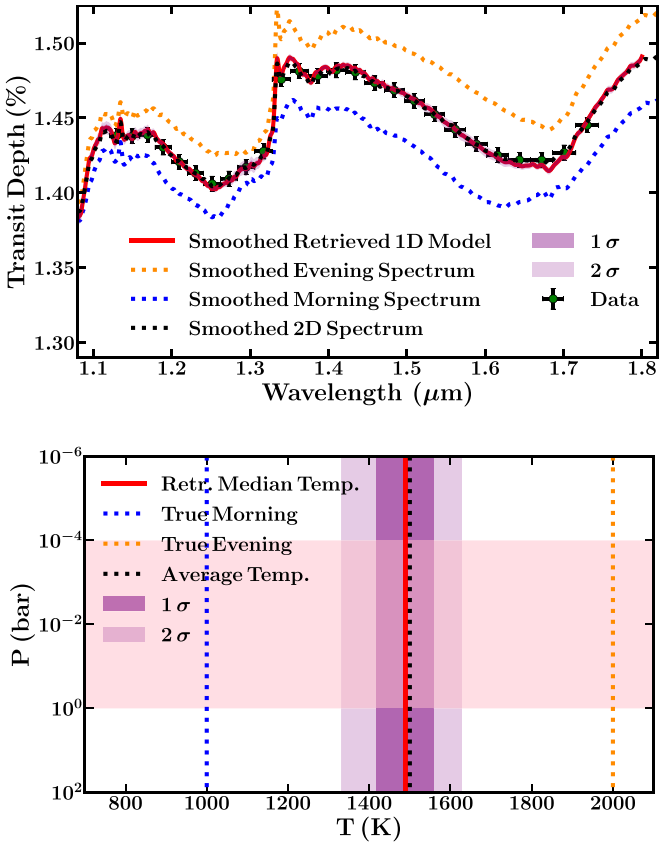

Figure 2. Retrieved results using a semi-analytic 1D model on a semi-analytic 2D synthetic data set. Top: Retrieved 1D transmission spectrum (red line) and synthetic observations (black error bars) from a 2D transmission spectrum (black dotted line). Colored dotted lines show the morning (blue) and evening (orange) spectra. Bottom: Red line shows the retrieved median 1D temperature. Dotted lines show the morning (blue) and evening (orange) input temperatures, as well as their average (black). Pink horizontal shaded region shows the estimated photospheric pressure range from MGL20. Retrieved 1σ and 2σ confidence intervals in the transmission spectrum and P–T profile are shown using purple shaded regions. Confidence intervals on the transmission spectrum are not visible, due to their narrow range.

and evening temperatures. The abundance and reference pressure are unconstrained and degenerate with each other. In order to break this degeneracy in semi-analytic models and derive a single chemical abundance, one must assume a reference pressure (Lecavelier Des Etangs et al. 2008a). For illustration, we perform a second retrieval assuming an arbitrary reference pressure of 0.1 bar for a radius of $R_{\rm p,ref} = 1.33182 R_{\rm J}$.

Figure 4 shows the posterior distributions from the retrieval assuming a reference pressure of 10 bar. With these input values, the 1D chemical abundance from Equation (6) is expected to be $\log_{10}(X_{\rm H_2O}) = -4$, as derived in Appendix A.1. Our retrieval finds $T_{\rm 1D} = 1485^{+71}_{-75}$ and $\log_{10}(X_{\rm H_2O}) = -4.0^{+0.1}_{-0.1}$, consistent with expectations. The retrieved transmission spectrum and P–T profile are virtually unchanged from the ones shown in Figure 2.

Overall, these semi-analytic retrievals confirm the intuition derived from the semi-analytic derivation included in Appendix A. When equating semi-analytic 1D and 2D models, the temperature from the 1D model is the average temperature of the two terminators in the 2D model. Our results contrast with the properties of the analytic expression from MGL20,

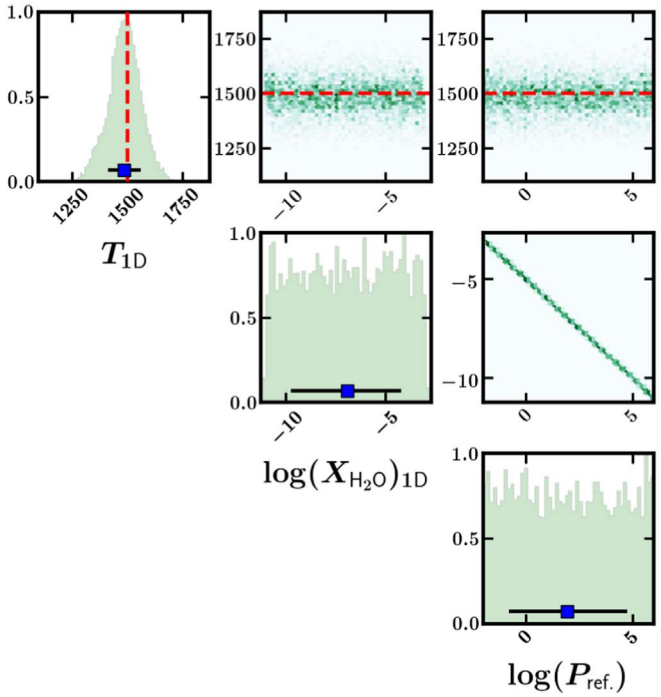

Figure 3. Posterior distributions for the retrieval using a semi-analytic 1D model on a semi-analytic 2D synthetic data set without assuming a reference pressure. The green histograms show the retrieved 1D isothermal temperature, 1D H_2O mixing ratio, and 1D reference pressure. The expectation (red line) from our semi-analytic derivation is $T_{\rm 1D} = \bar{T} = 1500$ K. Without assumptions about the reference pressure in the 1D model, the semi-analytic treatment expects a degeneracy between the chemical abundance and reference pressure. The retrieval matches the expectations from our semi-analytic treatment.

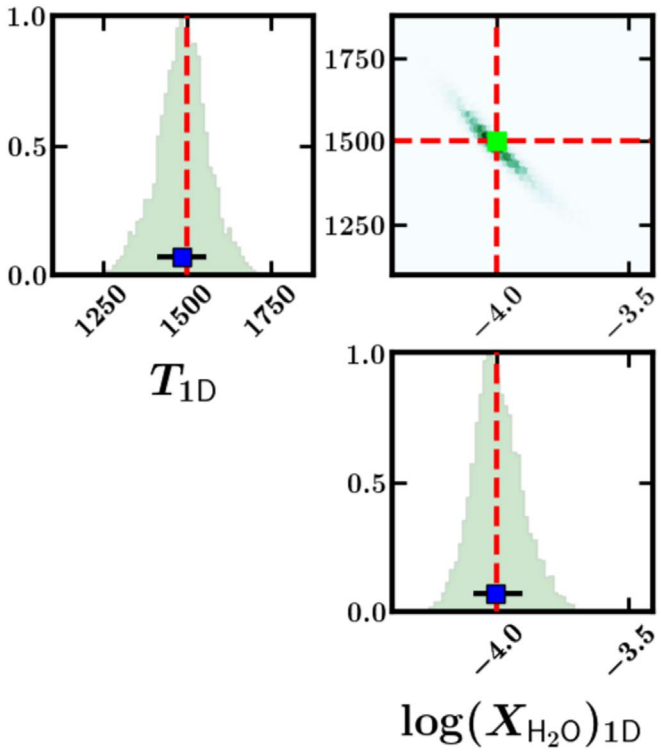

Figure 4. Same as Figure 3, but for the retrieval assuming a reference pressure in the 1D model of 0.1 bar. The expectations (red lines) from our semi-analytic derivation are $T_{\rm 1D} = \bar{T} = 1500$ K, and $\log_{10}(X_{\rm H_2O}) = -4$. The retrieval matches the expected values.

Table 2
Morning and Evening Chemical and Thermal Parameters for Selected Case Studies

Atmospheric Case	WJ Morning	WJ Evening	HJ Morning	HJ Evening	UHJ Morning	UHJ Evening
$\log_{10}(X_{H_2O})$	−3.3	−3.3	−3.3	−3.3	−3.3	−3.3
$\log_{10}(X_{Na})$	−8.0	−6.0	−6.0	−6.0	−6.0	−6.0
$\log_{10}(X_{K})$	−9.0	−7.0	−7.0	−7.0	−7.0	−7.0
$\log_{10}(X_{CH_4})$	−4.0	−6.0	N/A	N/A	N/A	N/A
$\log_{10}(X_{TiO})$	N/A	N/A	N/A	−7.0	N/A	N/A
$\log_{10}(X_{VO})$	N/A	N/A	N/A	−8.0	N/A	N/A
$\log_{10}(X_{H^-})$	N/A	N/A	N/A	N/A	N/A	−8.0
α_1	0.6	0.7	0.6	0.7	0.5	0.7
α_2	0.5	0.6	0.5	0.6	0.4	0.6
$\log_{10}(P_1)$	−2.0	−2.0	−2.0	−2.0	−2.0	−2.0
$\log_{10}(P_2)$	−5.0	−5.0	−5.0	−5.0	−5.0	−5.0
$\log_{10}(P_3)$	1.0	1.0	1.0	1.0	1.0	1.0
T_{deep}	1600	1600	2200	2200	3000	3000

Notes. The warm Jupiter (WJ), hot Jupiter (HJ), and ultra-hot Jupiter (UHJ) selected cases are constructed with the system and bulk properties of the prototypical hot Jupiter HD 209458b, and assume a reference radius of $R_{p,10bar} = 1.33182R_J$ at a reference pressure of $P_{ref} = 10$ bar. N/A means that the parameter is not included in the model by design. Models' parameters adopted from MGL20.

and three of their important takeaways in particular. First, MGL20 claim that compositional differences exceeding a factor of 2 (i.e., $\Delta \log_{10}(X) > 0.3$) like the one in our example ($\Delta \log_{10}(X) = 3.0$) result in biases many hundreds of degrees cooler than the average temperature of the two terminators. We find that, even in this case where the compositional difference is a factor of 1000, we retrieve a temperature consistent with the average temperature of the morning and evening terminators. Second, MGL20 claim that the wavelength dependency in their derived analytic expression implies that no one equivalent temperature can perfectly reproduce a 2D spectrum using a 1D model. Our results find that using this semi-analytic approach, a 1D model can reproduce a 2D spectrum. Third, MGL20 highlight that their semi-analytic derivation predicts $T_{1D} < \frac{1}{2}(T_E + T_M)$ under the assumption that the retrieved 1D mixing ratio is the average of the morning and evening abundances. Our results and analytic derivation indicate that the 1D volume mixing ratio in the semi-analytic treatment is not expected to be the average of the morning and evening mixing ratios. Finally, our results recover the well-known degeneracy between abundances and reference pressure from simplistic semi-analytic models.

Semi-analytic models and retrievals remain powerful tools to help build our understanding of transmission spectra. Nonetheless, when looking for more physically realistic models that incorporate multidimensional thermal and compositional inhomogeneities, the results of semi-analytic formalisms can be misleading. As comprehensively discussed in Welbanks & Madhusudhan (2019), simplified semi-analytic models are inadequate for reliable interpretations of transmission spectra. Instead, numerical models that relax some of these unphysical assumptions can be better tools in our analysis of exoplanet atmospheres. As such, we now investigate the retrieved atmospheric temperatures for 2D spectra using 1D models within a numerical atmospheric retrieval framework.

4. 1D Atmospheric Retrievals with Synthetic Observations

We explore the possibility of thermal and compositional biases resulting from retrieving the atmospheric properties of an exoplanet with asymmetric terminators (i.e., a 2D transmission spectra) using 1D atmospheric models within a numerical Bayesian atmospheric retrieval framework. Using synthetic observations, we appraise the performance of three different model families: (1) models as in MGL20 using a modified *P–T* parameterization and assuming a clear atmosphere; (2) models using the *P–T* parameterization of Madhusudhan & Seager (2009) and assuming a clear atmosphere; and (3) models using the *P–T* parameterization of Madhusudhan & Seager (2009) and including the presence of inhomogeneous clouds and hazes as described in Welbanks & Madhusudhan (2021), equivalent to the current state of the art in the field. We select three diverse cases with thermal and compositional differences ranging from warm Jupiters ($T_{eq} \sim 1000$ K) to ultra-hot Jupiters ($T_{eq} \sim 2500$ K). To allow for a direct comparison with MGL20 and their assumptions, we adopt their proposed atmospheric case studies summarized in Table 2.

4.1. Generating Synthetic Observations

We generate synthetic HST-STIS and HST-WFC3 observations assuming spectral resolutions and precisions comparable to current observations (e.g., Sing et al. 2016). To avoid possible biases due to different data generation procedures, we adopt the same parameters and procedure as MGL20. First, we generate a higher-resolution ($R \sim 2000$) spectrum from 0.3–2.0 μm solving line-by-line radiative transfer in transmission geometry in a plane-parallel atmosphere for each terminator (morning and evening). The model atmosphere for each terminator is discretized into 81 pressure layers uniformly spaced in $\log_{10}(P)$ from 10^{-6} to 10^{2} bar under hydrostatic equilibrium. The high-resolution spectra are linearly combined to construct a 2D transmission spectrum. Each 2D spectrum is then convolved using the point-spread function of the HST STIS G430/G750 gratings and HST-WFC3 G141 grisms and integrated over the sensitivity function of each instrument (see binning strategy in Section 2.1.6 in Pinhas et al. 2018). The assumed spectral resolutions and precisions are $R_{HST-STIS} = 20$ and 100 ppm, respectively, for HST-STIS, and $R_{HST-WFC3} = 60$ and 50 ppm for HST-WFC3. The observations do not include Gaussian scatter, following MGL20.

4.2. Retrieval Setup

The atmospheric retrievals are performed using Aurora (Welbanks & Madhusudhan 2021). The atmospheric model computes line-by-line radiative transfer in transmission geometry for a plane-parallel planet atmosphere under hydrostatic equilibrium (see, e.g., Pinhas et al. 2018; Welbanks & Madhusudhan 2021). The parameter estimation is performed using the nested sampling algorithm MultiNest (Feroz et al. 2009, 2019), through PyMultiNest (Buchner et al. 2014). Each retrieval is performed using 4000 nested sampling live points. We consider three model configurations:

1. MGL20: These models follow the procedure of MGL20 where the *P–T* profile is parameterized using a modification to the parameterization of Madhusudhan & Seager (2009). That is, instead of retrieving the temperature at the top of the atmosphere (T_0) like Madhusudhan & Seager (2009), MGL20 retrieve the temperature at 10 bar ($T_{\rm deep}$). These models retrieve the reference planetary radius at a reference pressure of 10 bar ($R_{\rm p,10\ bar}$), and assume a clear atmosphere.
2. Clear atmosphere: These models follow the standard retrieval procedure explained in Welbanks & Madhusudhan (2021) for a clear atmosphere. The *P–T* parameterization follows the prescription of Madhusudhan & Seager (2009). The reference pressure is retrieved for the reference radius used in the morning and evening models.
3. Cloudy atmosphere: These models follow the same procedure as the clear atmosphere models, but include the possibility of clouds and hazes using the generalized prescription of Welbanks & Madhusudhan (2021). The parameterization considers the possibility of four different sectors: (1) a clear sector, (2) a sector with hazes only, (3) a sector with clouds only, and (4) a sector with clouds and hazes. Clouds are included by a pressure parameter ($P_{\rm cloud}$) that determines the pressure level at which the atmosphere becomes optically thick due to the presence of a cloud deck. Hazes are included as a deviation from H_2 Rayleigh scattering using a parametric cross section $\sigma_{\rm hazes} = a\sigma_0(\lambda/\lambda_0)^{\gamma}$, where γ is the scattering slope, a is the Rayleigh-enhancement factor, and σ_0 is the H_2 Rayleigh-scattering cross section (5.31×10^{-31} m^2) at a reference wavelength λ_0 (350 nm). The fractional cover of each of the four sectors above is a free parameter and follows the unit-sum constraint (i.e., $\phi_{\rm clear} = 1 - \phi_{\rm hazes} - \phi_{\rm clouds} - \phi_{\rm clouds+hazes}$).

To avoid biases due to different pressure grids between models, we maintain the choice of 81 pressure levels from 10^{-6} to 10^{2} bar of MGL20 for all model configurations. The retrievals include as free parameters the abundances of the chemical species used as input in each of the atmospheric cases (i.e., warm Jupiter: H_2O, Na, K, and CH_4; hot Jupiter: H_2O, Na, K, TiO, and VO; ultra-hot Jupiter: H_2O, Na, K, H^-). The sources of opacity included are H_2-H_2 and H_2-He CIA (Richard et al. 2012), H_2O (Rothman et al. 2010), CH_4 (Yurchenko et al. 2013; Yurchenko & Tennyson 2014), Na (Allard et al. 2019), K (Allard et al. 2016), TiO (Kurucz 1992; Schwenke 1998; Hill et al. 2013), VO (McKemmish et al. 2016), and bound–free H^- (John 1988), with their computation following the methods and descriptions in Gandhi & Madhusudhan (2017, 2018), Gandhi et al. (2020b, 2020a), and Welbanks et al. (2019). The priors, summarized in Appendix B, Table B1, are generally standardized and follow the description of MGL20 for the MGL20 models and Welbanks & Madhusudhan (2021) for the clear and cloudy models. We choose to retrieve the reference pressure instead of the reference radius, as the planetary radius is generally the observable quantity.

4.3. Retrieval Results

The retrieved *P–T* profiles from our retrievals are shown in Figure 5, while the retrieved spectra and posterior distributions are included in Appendix C, Figures C1 and C2. First, our reproduction of the results from MGL20 are consistent with their findings. When using the *P–T* parameterization from MGL20, the retrieved photospheric temperatures ($T_{1\ \rm bar}$ to $T_{0.1\ \rm mbar}$) are generally cooler than the average of their morning and evening terminator temperatures. For the warm Jupiter case, the average temperature is consistent within the 2σ confidence contour of the retrieved estimates for $P \lesssim 0.01$ bar. The retrieved temperature estimates for the deeper atmosphere are inconsistent with the average temperature with discrepancies of $\sim$200 K at $P \sim 1$ bar. The hot Jupiter case is similar, with a similar discrepancy of $\sim$200 K between the retrieved 2σ confidence contour and the average temperature at $P \sim 1$ bar. Finally, the largest bias is found in the ultra-hot Jupiter scenario, for which the retrieved temperature and associated confidence intervals are inconsistent with the average temperature. The 2σ confidence interval and the average temperature are inconsistent at $P \sim 1$ bar to $\gtrsim$1000 K.

Our reproduction of MGL20 also obtains the compositional biases they highlight, as well as the relatively poor constraints of Na and K for the hot and ultra-hot Jupiter scenarios. Although the spectral fits (top row, Figure C1) are generally a good fit to the data, the retrieved abundances (top row, Figure C2) can be inconsistent with the expectation of average chemical abundances to within 1σ for the warm and hot Jupiter scenarios. On the other hand, the ultra-hot Jupiter results show a worse spectral fit, and the retrieved abundances of H_2O and H^- can be inconsistent with the assumption of average chemical assumptions above 3σ.

Next, we perform a retrieval using our standard setup for clear atmospheres using the *P–T* parameterization from Madhusudhan & Seager (2009). The results are shown in the middle row of Figure 5 and Figures C1 and C2 in Appendix C. The retrieved *P–T* profiles for this model are somewhat less biased than those obtained using the MGL20 *P–T* parameterization. The discrepancy between the 2σ confidence interval, and the average temperature at $P \sim 1$ bar is $\sim$100 K for the warm and hot Jupiter cases. Similarly, the retrieved temperatures at the slant photosphere ($P \sim 10^{-3}$–10^{-1} bar, e.g., Welbanks & Madhusudhan 2019) are generally consistent with the average temperature of the morning and evening terminators within the 2σ confidence intervals to within 100 K.

On the other hand, the ultra-hot Jupiter temperature estimates at the transmission spectroscopy photosphere remain inconsistent, although to a lesser degree. The difference between the 2σ confidence interval and the average temperature for the ultra-hot Jupiter is $\lesssim$350 K at most pressures. The retrieved transmission spectra (middle panel of Figure C1) for the clear model shows a reasonably good fit to the synthetic observations, with a worse fit for the ultra-hot Jupiter case in the optical wavelengths. The retrieved chemical abundances (middle panel of Figure C2) remain mostly unchanged from those retrieved

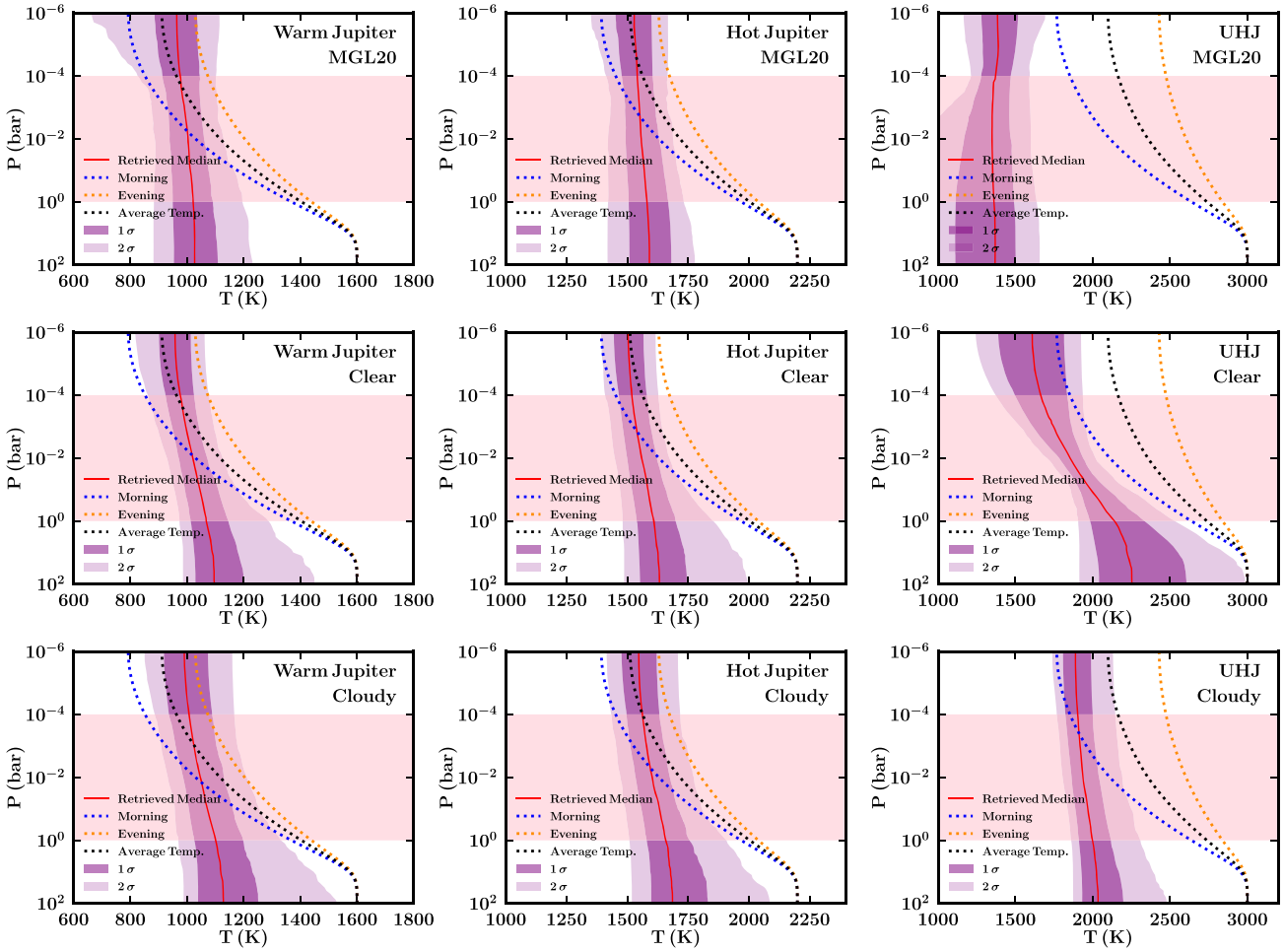

Figure 5. Retrieved *P–T* profiles from our numerical retrievals using 1D models on synthetic data from a 2D model. Each column corresponds to an atmospheric case adopted after MGL20: a warm Jupiter ($\bar{T} \sim 1000$ K), a hot Jupiter ($\bar{T} \sim 1600$ K), and an ultra-hot Jupiter ($\bar{T} \sim 2200$ K). Each row corresponds to a different model strategy: a clear atmospheric model with the *P–T* parameterization from MGL20 (top), a cloud-free model using the *P–T* parameterization from Madhusudhan & Seager (2009; middle), and a model with inhomogeneous clouds and hazes and the *P–T* parameterization from Madhusudhan & Seager (2009; bottom). The true morning (blue) and evening (orange) *P–T* profiles used to generate the 2D model and synthetic data, along with their average (black), are shown using dotted lines. The retrieved median (red line) and 1σ and 2σ confidence intervals (purple shaded regions) are shown. Pink horizontal shaded region shows the estimated photospheric pressure range from MGL20.

with the MGL20 models, with the exception of H^- in the ultra-hot Jupiter case, which is consistent with the average of the morning and evening terminators. The retrieved Na and K abundances are relatively unconstrained in the hot and ultra-hot Jupiter cases.

The results from our models with inhomogeneous clouds and hazes are shown in the bottom row of Figures 5, C1, and C2. The retrieved *P–T* profile estimates from the cloudy models for the warm and hot Jupiter cases are largely consistent with the average temperature of the two terminators near the slant photosphere ($P \sim 10^{-3}$–10^{-1} bar). The average temperature is marginally consistent with the retrieved 2σ contour at $P \sim 1$ bar to within $\lesssim$100 K for the warm and hot Jupiter cases. The ultra-hot Jupiter temperature estimates are consistent with the average temperature for $P \lesssim 0.1$ mbar, and inconsistent at $\lesssim$450 K for higher pressures up to $\sim$1 bar.

The cloudy models retrieved spectra that are in good agreement with the synthetic data for all planet scenarios. Although our models allow for the possibility of clouds and hazes, the retrieved solutions correctly indicate that the input data correspond to a cloud-free atmosphere (i.e., $\phi_{\rm hazes} \sim 0$, $\phi_{\rm clouds} \sim 0$, $\phi_{\rm clouds+hazes} \sim 0$). Furthermore, the retrieved chemical abundances are consistent with the average of the abundances of the morning and evening terminators within $\sim 1\sigma$ for the warm and hot Jupiter cases, even though the retrieved abundances may not strictly be expected to be the average of the two terminators. The retrieved H_2O and H^- abundances for the ultra-hot Jupiter scenario are consistent with the average of the two terminators at $\sim 3\sigma$. Importantly, the retrieved posterior distributions for some chemical abundances begin to show multimodal behavior. Observing such modes in a posterior distribution would indicate that we should be careful with our interpretation of the retrieved median abundance and not treat that value as a reliable indication of the overall abundance of the planet (see, e.g., WASP-39b in Welbanks et al. 2019).

Even for the most extreme case of an ultra-hot Jupiter, our photospheric temperature discrepancy of $\lesssim$450 K from the true average at the 2σ boundary is still significantly lower than that of MGL20. Nevertheless, it is important to establish the cause of any such discrepancy. An inspection of the model behind the synthetic observations for this case, following MGL20, offers

some insights. The third column in Figure C1 shows the evening and morning spectra that formed the 2D input spectrum via linear combination. The evening terminator has almost no visible spectral features in the optical, due to the high H^- abundance assumed in the case study, resulting in an almost flat spectrum. On the other hand, the morning terminator spectrum has clear Na, K, and H_2O features. Therefore, the ultra-hot Jupiter scenario is a pathological scenario due to its almost featureless evening spectrum.

It is also important to note that parts of both terminators face the same sides (i.e., the day or the night side). Compositional and temperature inhomogeneities may be expected to be stronger across the day–night boundary than the morning–evening boundary as considered here. The biases uncovered by this pathological case may therefore be representative of only the most extreme of cases and not of the broader hot Jupiter population. Nevertheless, we still address this extreme case with a new retrieval framework in Section 6.

Overall, our results find that the modified *P–T* profile used by MGL20 results in temperature estimates that are cooler by a factor of ∼2 or more compared to the other cases we consider. On the other hand, the models using the *P–T* parameterization from Madhusudhan & Seager (2009) find retrieved temperatures near the photosphere for transmission spectroscopy largely consistent with the average of the two terminators for the warm and hot Jupiter scenarios, and a smaller thermal bias for the ultra-hot Jupiter. Finally, the inclusion of inhomogeneous clouds and hazes in the atmospheric models results in chemical abundances that are less biased than those obtained with the cloud-free models.

5. 1D Atmospheric Retrievals with Existing Observations

We extend our investigation into the origin of thermal anomalies by revisiting published transmission spectra for which previous studies have inferred anomalously cool atmospheric temperatures. We choose two planets with widely different temperatures and for which broad optical to infrared observations are available. In particular, we revisit recent inferences on the atmospheric properties of the hot Jupiter WASP-43b (Hellier et al. 2011) and ultra-hot Jupiter WASP-103b (Gillon et al. 2014) made by Weaver et al. (2020) and Kirk et al. (2021), respectively. We revisit their reported inferences, reproduce them using their model assumptions where possible, and perform additional retrievals using the full model setup discussed above to resolve biases.

5.1. The Hot Jupiter WASP-43b

Weaver et al. (2020) performed an atmospheric retrieval of the hot Jupiter WASP-43b using a ground-based optical transmission spectrum ($\lambda = 0.53$–$0.9\,\mu$m) obtained as part of the ACCESS Survey on Magellan/IMACS, in combination with HST-WFC3 observations from Kreidberg et al. (2014b). Their atmospheric retrieval framework, adapted from the work of Espinoza et al. (2019), assumes an isothermal and isobaric atmosphere following semi-analytic treatments (e.g., Bétrémieux & Swain 2017; Heng & Kitzmann 2017). Their results find no evidence for chemical absorbers such as Na and K in the optical, but confirm the presence of H_2O in the atmosphere of the planet, with abundances consistent with previous results (e.g., Kreidberg et al. 2014b). Furthermore, their results suggest the presence of star spots on the surface of WASP-43 impacting the transmission spectrum of the planet. Nonetheless, they retrieve an isothermal temperature for the atmosphere of the planet of $T_{\rm iso.} = 352.91^{+206.14}_{-125.08}$ K, an estimate considerably cooler than the equilibrium temperature of the planet $T_{\rm eq} = 1440$ K (e.g., Welbanks & Madhusudhan 2021) and expectations from GCM studies (e.g., Kataria et al. 2015).

5.1.1. Retrieval Setup

Weaver et al. (2020) employ simplified semi-analytic models with isothermal and isobaric assumptions. The limitations of these models, and their impact on retrieved atmospheric properties, has been extensively discussed in Welbanks & Madhusudhan (2019). Although their general retrieval setup is presented, some key aspects of their modeling strategy are not self-evident (e.g., the complete list of chemical species considered and whether collision-induced absorption was included). As a result, we do not perform a direct reproduction of their results using semi-analytic models, nor are we able to incorporate their exact modeling assumptions into our numerical 1D models. Instead, we perform a numerical retrieval relaxing the isothermal and isobaric assumptions of their semi-analytic model. We employ the *P–T* parameterization of Madhusudhan & Seager (2009) with the same priors as Welbanks et al. (2019; e.g., as shown in Table B1, except for T_0, which follows a uniform prior between 800 K and 1540 K).

Our retrieval for WASP-43b follows the general description presented in Section 4.2. The parameter estimation is performed using PyMultiNest (Buchner et al. 2014) with 2000 nested sampling live points. Our model considers free parameters for the volume mixing ratios of different chemical species, the possibility of inhomogeneous clouds and hazes, and a parameterization for the *P–T* profile of the planet.

The retrieval in Weaver et al. (2020) does not consider nonuniform cloud cover. Instead, they interpret their retrieved reference pressure as a cloud-top pressure that indicates the transition between an optically thin and an optically thick atmosphere due to clouds. Additionally, Weaver et al. (2020) include the presence of hazes using the parameterization explained in Section 4.2 and in Lecavelier Des Etangs et al. (2008a), MacDonald & Madhusudhan (2017), Pinhas et al. (2018), Welbanks & Madhusudhan (2019), and Welbanks & Madhusudhan (2021). Our retrieval considers the presence of clouds and hazes following the description in Section 4.2, with the full four-sector generalized parameterization of Welbanks & Madhusudhan (2021) for nonuniform cloud/haze cover.

Weaver et al. (2020) explore the impact of stellar heterogeneities by following the formalism described in Rackham et al. (2018, 2019) and Pinhas et al. (2018). We do the same using the functionalities in Aurora inherited from AURA (Pinhas et al. 2018). We adopt a uniform prior for the spot fraction between 0 and 0.5, a uniform prior in the spot temperatures between 0.6 and 1.2 times the stellar effective temperature (i.e., $T_{\rm eff.} = 4520$ K; see, e.g., Gillon et al. 2012), and a Gaussian prior for the photospheric temperature with a mean of $T_{\rm eff.} = 4520$ K and standard deviation of 120 K informed by Gillon et al. (2012).

In agreement with Weaver et al. (2020), we also include a free parameter to retrieve an instrumental shift between the optical and infrared observations. We use a Gaussian prior with a standard deviation of 1000 ppm, similar to Weaver et al. (2020), and a mean of 0 ppm. We consider absorption due to H_2O, Na, K, CH_4, NH_3, CO, CO_2, TiO, and VO, with a log-

uniform prior on their volume mixing ratios from −16 to −1. Our retrieval uses the optical data from Weaver et al. (2020), the HST-WFC3 observations from Kreidberg et al. (2014b), the Spitzer transit depths at 3.6 μm and 4.5 μm from Stevenson et al. (2017), and input system parameters from Gillon et al. (2012).

5.1.2. Retrieval Results

Our retrieval of the optical and infrared transmission spectrum of the hot Jupiter WASP-43b suggests the presence of H_2O ($\sim 2\sigma$), a strong preference for an offset between the optical and infrared observations ($\sim 7\sigma$), and evidence for stellar contamination in the optical transmission spectrum ($\sim 4\sigma$). Figure 6 shows the retrieved transmission spectrum and the retrieved *P–T* profile. Our retrieved transmission spectrum is in good agreement with the observations. Furthermore, our retrieved *P–T* profile has a temperature near the slant photosphere ($P \sim 10^{-3}$–10^{-1} bar) consistent with the equilibrium temperature of the planet ($T_{\rm eq} = 1440$ K) within $\sim 1\sigma$.

Our retrieved H_2O volume mixing ratio of $\log_{10}(X_{H_2O}) = -5.27^{+0.61}_{-0.46}$ is consistent within $\sim 1\sigma$ with previous estimates using infrared observations only (e.g., Kreidberg et al. 2014b; Welbanks et al. 2019), and lower than the estimate from Weaver et al. (2020) not using the Spitzer transit depths (i.e., $\log_{10}(X_{H_2O}) = -2.78^{+1.38}_{-1.47}$). Our retrieval suggest the presence of stellar heterogeneities in the transmission spectrum, as the result of spots with an average temperature of $T_{\rm het.} = 4102.84^{+86.99}_{-99.56}$, ~300 K cooler than the retrieved stellar photosphere $T_{\rm phot.} = 4484.76^{+82.72}_{-72.46}$, with a cover fraction of $\delta = 0.11^{+0.05}_{-0.03}$. These estimates are generally consistent with the retrieved parameters of Weaver et al. (2020).

Additionally, we retrieve an offset of $f_{\rm offset} = 847^{+133}_{-128}$ ppm between the optical and infrared observations. Weaver et al. (2020) retrieve an offset of $f_{\rm offset} = 25749.40^{+101.54}_{-105.70}$ ppm. Considering the mean white light-curve depth of 25,071 ppm derived by Weaver et al. (2020), their retrieved offset translates to a value of $f_{\rm offset} = 678.40^{+101.54}_{-105.70}$ ppm, which is consistent with our estimate to within 1σ. We note, however, that our retrieval includes both HST-WFC3 and Spitzer observations, whereas Weaver et al. (2020) use only HST-WFC3 in the infrared.

Our retrieved *P–T* profile is largely consistent with the equilibrium temperature of the planet $T_{\rm eq} = 1440$ K (e.g., Welbanks & Madhusudhan 2021). The retrieved temperature at 100 mbar, near the photosphere, is $T_{\rm 100\,mbar} = 1257^{+235}_{-214}$ K and consistent with the equilibrium temperature of the planet within 1σ. Additionally, the retrieved temperature at 100 mbar falls within the range of temperatures at ~100 mbar found for the same planet by Kataria et al. (2015) using GCMs. Figure 6 also shows the retrieved isothermal temperature of $T_{\rm iso.} = 352.91^{+206.14}_{-125.08}$ K from Weaver et al. (2020). Our retrieved median temperature at 100 mbar is ~900 K warmer than the median retrieved temperature of Weaver et al. (2020).

We further assess whether our models preferentially explain the optical data using models that consider the impact of stellar heterogeneities or the presence of inhomogeneous clouds and hazes. Weaver et al. (2020) find that, given current data quality, it is not possible to fully distinguish between the impact on the spectrum due to hazes and the contamination from stellar heterogeneities. We find no preference for models with clouds and hazes relative to models without. Our retrieved cloud and haze properties are unconstrained and largely suggestive of an atmosphere with low cloud and haze cover (i.e., $\phi_{\rm clouds} \approx \phi_{\rm hazes} \approx \phi_{\rm clouds+hazes} \approx 0$). These results suggest that the data are preferentially explained by contamination from an inhomogeneous stellar photosphere instead of inhomogeneous cloud and haze cover. Future observations could better inform these poor constraints on the cloud and haze properties of WASP-43b.

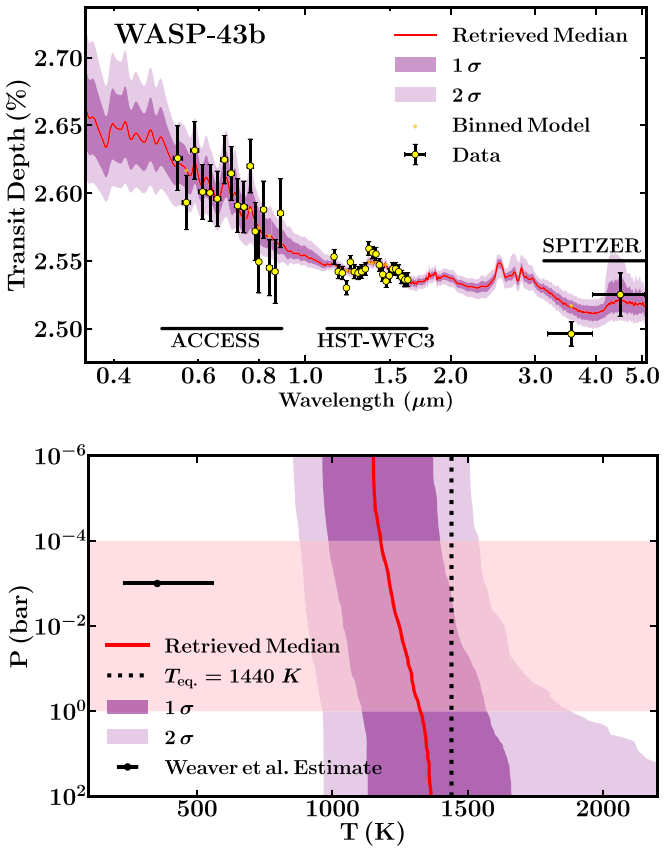

Figure 6. Results for the retrieval of ACCESS, HST-WFC3, and Spitzer WASP-43b data from Weaver et al. (2020), Kreidberg et al. (2014b), and Stevenson et al. (2017). Top: Retrieved median transmission spectrum (red line) and 1σ and 2σ confidence intervals (purple shaded regions) are shown alongside the observations (error bars) and binned median model (diamonds). Bottom: Retrieved median *P–T* profile (red line) and 1σ and 2σ confidence intervals (purple shaded regions). Pink horizontal shaded region shows the estimated photospheric pressure range from MGL20. Horizontal error bar shows the median and 1σ retrieved temperature from Weaver et al. (2020). Our retrieved temperature is consistent with the equilibrium temperature of the planet ($T_{\rm eq} = 1440$ K, dotted line).

Our results indicate that the use of semi-analytic models with isothermal and isobaric assumptions[4] by Weaver et al. (2020) may have biased their atmospheric temperature estimates, leading to cooler temperatures inconsistent with expectations for the atmospheric temperature of the planet. On the other hand, our numerical models with height-dependent gravity, a parametric *P–T* profile, and inhomogeneous clouds and hazes result in temperature estimates consistent with the equilibrium temperature of the planet and GCM simulations. Our retrieval using the full numerical model suggests that the retrieved temperature biases from Weaver et al. (2020) for WASP-43b

[4] Failing to consider collision-induced absorption will additionally impact any atmospheric inferences (see, e.g., Welbanks & Madhusudhan 2019). If that is the case for the semi-analytic models of Weaver et al. (2020), this assumption would have exacerbated any retrieved biases.

may likely be due to the use of simplified semi-analytic models, rather than due to biases in 1D retrievals applied to asymmetric terminators in hot Jupiters.

5.2. The Ultra-hot Jupiter WASP-103b

Kirk et al. (2021) use a ground-based optical transmission spectrum ($\lambda = 0.390$–$0.945\ \mu$m) from the ACCESS (Magellan/IMACS) and LRG-BEAST (William Herschel Telescope-ACAM) surveys, as well as archival data from Gemini-GMOS and VLT-FORS2, in combination with infrared HST-WFC3 and Spitzer data from Kreidberg et al. (2018), to infer the atmospheric properties of the ultra-hot Jupiter WASP-103b. Their atmospheric retrievals are performed using the frameworks petitRADTRANS (Mollière et al. 2019) for the optical transmission spectrum, and POSEIDON (MacDonald & Madhusudhan 2017) for the combined optical and infrared transmission spectrum. Their results with POSEIDON using the combined transmission spectrum find weak to no detections (i.e., $\lesssim 2.0\sigma$) of H_2O, TiO, and HCN. However, their results indicate a $\sim 4.0\sigma$ preference for models considering contamination in the spectrum from unocculted stellar heterogeneities. However, the retrieved isothermal atmospheric temperature for the full model using POSEIDON of $T_{\rm iso.} = 782^{+283}_{-231}$ K is lower than the equilibrium temperature of this ultra-hot Jupiter (e.g., $T_{\rm eq} = 2484$ K Delrez et al. 2018) and estimates from phase-curve observations and GCM simulations (e.g., Kreidberg et al. 2018).

5.2.1. Retrieval Setup

We perform two numerical atmospheric retrievals for our analysis of WASP-103b using ground- and space-base observations. First, we perform a reproduction of the "full" POSEIDON retrieval performed by Kirk et al. (2021). We use their same free parameters and priors, with the exception of their choice to retrieve a reference radius at 10 bar. Instead, we retrieve the reference pressure ($P_{\rm ref}$) at the planetary radius uncorrected for asphericity ($R_{\rm p} = 1.623\ R_{\rm J}$) used by Kirk et al. (2021). In total, our reproduction retrieval has 22 free parameters: 12 parameters for the volume mixing ratios[5] of Na, K, H^-, TiO, VO, AlO, CrH, FeH, H_2O, CO, CO_2, and HCN; one parameter for an isothermal P–T profile; one parameter for the reference pressure $P_{\rm ref}$ at a reference radius; four parameters for the presence of inhomogeneous clouds and hazes with the assumption of a single sector capturing their joint contribution (e.g., as in MacDonald & Madhusudhan 2017); three parameters for contributions from stellar heterogeneities as described above and in Pinhas et al. (2018); and one parameter for an instrumental shift between the optical and infrared observations.

Then, we perform a second retrieval of WASP-103b relaxing some of the assumptions made by Weaver et al. (2020). First, instead of using an isothermal P–T profile, we use the parameterization of Madhusudhan & Seager (2009) with priors as in Table B1, except for T_0, which follows a uniform prior between 800 K and 2584 K. Second, instead of using an unphysical prior on the volume mixing ratio of H^- (i.e., log-uniform from -16 to -1), we adopt a physically motivated prior where unrealistically high H^- abundances (i.e., $\log_{10}(X_{H^-}) > -7.0$, e.g., Parmentier et al. 2018) are not allowed, following a log-uniform distribution from -16 to -7. Third, we use as our reference radius the planetary radius corrected for asphericity ($R_{\rm p} = 1.681\ R_{\rm J}$) reported by Delrez et al. (2018). Fourth, we do not restrict the presence of clouds and hazes to a single sector, and instead use the more generalized parameterization for inhomogeneous clouds and hazes of Welbanks & Madhusudhan (2021) as explained in Section 4.2. All other parameters and priors remain as in the reproduction retrieval described above. For both retrievals, the parameter estimation is performed using PyMultiNest (Buchner et al. 2014) with 2000 nested sampling live points.

[5] The sources of opacity remain as described in Section 4.2, with the addition of Patrascu et al. (2015) for AlO; Bauschlicher et al. (2001) for CrH; Rothman et al. (2010) for CO and CO_2; Barber et al. (2014) for HCN; and Dulick et al. (2003), Wende et al. (2010), and Hargreaves et al. (2010) for FeH.

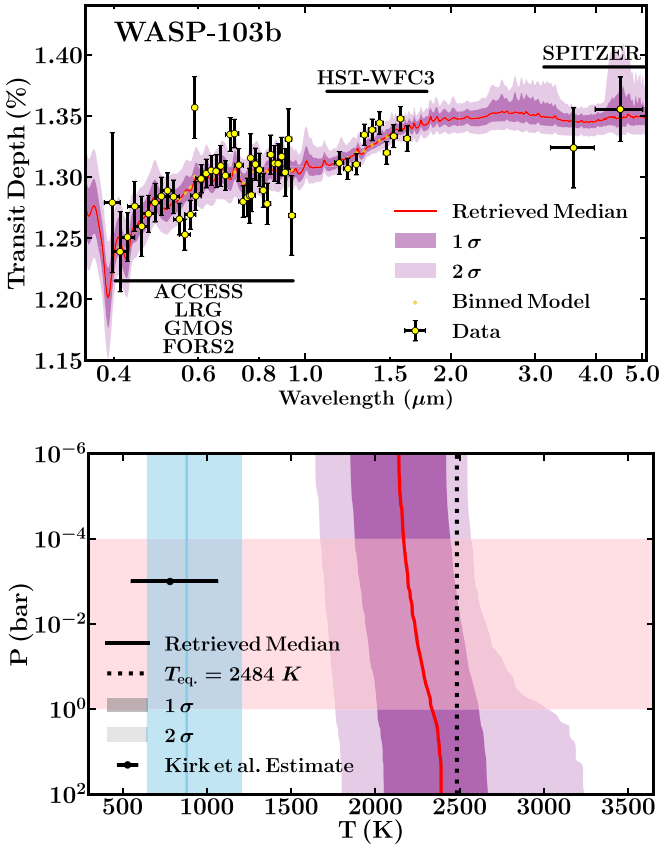

Figure 7. Results for the retrieval of ACCESS, LRG, Gemini-GMOS, VLT-FORS2, HST-WFC3, and Spitzer WASP-103b data from Kirk et al. (2021). Top: Retrieved transmission spectrum for our numerical retrieval of the planet, relaxing the assumptions from Kirk et al. (2021). Median transmission spectrum (red line) and 1σ and 2σ confidence intervals (purple shaded regions) are shown alongside the observations (error bars) and binned median model (diamonds). Bottom: Retrieved P–T profiles. Reproduction from Kirk et al. (2021) is shown using blue. Retrieval following our modeling procedure is shown in red. Median value is shown with the solid line, and confidence intervals with vertical shaded regions. Pink horizontal shaded region shows the estimated photospheric pressure range from MGL20. Horizontal error bar shows the median and 1σ retrieved temperature from Kirk et al. (2021). Our retrieved temperature is consistent with the equilibrium temperature of the planet ($T_{\rm eq} = 2484$ K, vertical dotted line).

5.2.2. Retrieval Results

Figure 7 shows the retrieved transmission spectrum from our full retrieval in the top panel. The bottom panel of Figure 7 shows the retrieved P–T profile from both the reproduction of the "full" retrieval with POSEIDON from Kirk et al. (2021) and our full reanalysis. The black horizontal error bar in Figure 7

shows the isothermal temperature estimate from Kirk et al. (2021).

Our reproduction of Kirk et al. (2021) finds poor constraints on the chemical abundances of most species considered. The retrieved abundances of $\log_{10}(X_{H_2O}) = -3.85^{+1.21}_{-4.21}$ and $\log_{10}(X_{TiO}) = -8.20^{+1.56}_{-1.61}$ are consistent with the abundances reported by Kirk et al. (2021). Their associated detection significances are 1.8σ and 1.9σ for H_2O and TiO, respectively. HCN is not detected (1.0σ preference), and its abundance is poorly constrained, with a retrieved volume mixing ratio of $\log_{10}(X_{HCN}) = -6.58^{+3.57}_{-5.61}$, consistent with the retrieved value from Kirk et al. (2021).

Similarly, the reproduction retrieval exhibits a strong preference for models considering stellar heterogeneity to a 4.6σ level. The retrieved faculae have a temperature of $T_{het} = 6498.43^{+202.80}_{-176.63}$ K and a cover fraction $\delta = 0.25^{+0.11}_{-0.09}$. The retrieved photospheric temperature is $T_{phot.} = 6187.70^{+111.74}_{-132.05}$ K. The retrieved parameters associated with stellar contamination are consistent with those retrieved by Kirk et al. (2021). Additionally, we retrieve an offset between the optical and infrared observations of $f_{shift} = 226^{+81}_{-95}$ ppm, consistent with the estimate from POSEIDON.

In agreement with Kirk et al. (2021), the retrieved isothermal temperature from our reproduction is cooler than the equilibrium temperature of the planet. The retrieved isothermal temperature $T_{iso.} = 862.70^{+292.98}_{-217.61}$ K has a median value ~1600 K cooler than the equilibrium temperature of $T_{eq} = 2484$ K. Our reproduction shows a general agreement with the results of Kirk et al. (2021), indicating a good agreement in our implementation of their model assumptions.

Next, we present the results from our full reanalysis with different model assumptions. Figure 7 shows that the retrieved spectrum is in agreement with the observations. Additionally, the bottom panel shows the agreement between the retrieved P–T profile and the equilibrium temperature of the planet. Our results find weak to no detections of TiO and H_2O with detection significances at the 1.3σ and 1.4σ levels, respectively. On the other hand, absorption due to HCN is not preferred by our models. In contrast, the retrieval indicates a strong preference for stellar heterogeneities in the spectrum at a 4.8σ level.

The retrieved chemical abundances are poorly constrained. The retrieved volume mixing ratios of $\log_{10}(X_{H_2O}) = -7.65^{+2.18}_{-5.14}$, $\log_{10}(X_{TiO}) = -9.84^{+0.87}_{-1.04}$, and $\log_{10}(X_{HCN}) = -10.82^{+3.22}_{-3.17}$ are consistent with the estimates of Kirk et al. (2021). Furthermore, the retrieved stellar contamination parameters suggest the presence of faculae with temperatures of $T_{het.} = 6653.62^{+313.47}_{-251.27}$ K covering $\delta = 0.20^{+0.10}_{-0.08}$, ~400 K hotter than the retrieved photospheric temperature $T_{phot.} = 6205.64^{+119.50}_{-128.52}$ K, consistent with those from Kirk et al. (2021).

Our reanalysis finds a temperature near the photosphere of $T_{100\,mbar} = 2313^{+279}_{-308}$, consistent with the equilibrium temperature ($T_{eq} = 2484$ K) within 1σ. Additionally, this retrieved temperature is consistent with the photospheric temperature estimates inferred from phase-curve observations of the same planet (e.g., Kreidberg et al. 2018). This non-isothermal model finds warmer temperatures than the isothermal temperature of $T_{iso.} = 782^{+283}_{-231}$ K inferred by Kirk et al. (2021) and shown in Figure 7. Overall, our results suggest that the previously retrieved cooler temperatures for this ultra-hot Jupiter are likely the result of assumptions in the models employed, rather than asymmetric terminators affecting 1D models.

6. A 2D Retrieval Framework for Asymmetric Terminators

An important next step in the development of atmospheric models is the development of models capable of capturing the properties of planets with asymmetric terminators. Toward this end, we demonstrate a multidimensional (1D+1D), referred to here as 2D, retrieval framework for exoplanetary transmission spectra. Our model explores the atmospheric properties of the morning and evening terminators of an exoplanet using a linear combination of atmospheric models. This is, to the best of our knowledge, the first implementation of a "free retrieval" (i.e., not restricted by chemical equilibrium assumptions) for exoplanet transmission spectra. We note, however, that the use of linear combinations to model exoplanetary inhomogeneities was first introduced by Line & Parmentier (2016). Additionally, this approach to model the morning and evening terminators of exoplanets was recently implemented by Espinoza & Jones (2021) using the retrieval framework CHIMERA (Line et al. 2013), although with constraints of chemical equilibrium and forcing thermal inhomogeneities between terminators. Unlike our general approach described below, Espinoza & Jones (2021) restrict their models to the cases in which the contribution of each terminator to the final spectrum is 1/2. Our implementation uses the existing Aurora framework (Welbanks & Madhusudhan 2021) due to its modular and multidimensional functionalities. In what follows, we describe our 2D implementation and assess its performance on the synthetic observations of asymmetric terminators generated above.

6.1. A 2D Model for Asymmetric Terminators

We expand the atmospheric models in Aurora to include 1D +1D models for asymmetric terminators, which we refer to as 2D models. These 2D models are the result of solving numerically for the transit depth of each terminator and calculating their linear combination. The transit depth for each terminator T_i is given by

$$\Delta_{\lambda,T_i} = \frac{R_p^2 + \int_{R_p}^{R_p+H_{A,T_i}} 2b(1 - e^{-\tau_{\lambda,T_i}(b)})db - \int_0^{R_p} 2be^{-\tau_{\lambda,T_i}(b)}db}{R_{star}^2}, \quad (7)$$

where R_p is the planetary radius, R_{star} is the stellar radius, and $H_{A,Ti}$ and τ_{λ,T_i} are the maximum height of the planetary atmosphere and the slant optical depth at terminator T_i, respectively. We maintain the choice of Welbanks & Madhusudhan (2021) to show Equation (7) as a three-part integral in order to emphasize that the chosen R_p may not correspond to an optically thick part of the atmosphere. The choice of R_p and associated P_{ref} can be different for each terminator. However, for this work we perform an initial appraisal for which the reference pressure P_{ref} and reference radius R_p pair act as a shared anchor point for the pressure and radial grids of both atmospheric models.

The calculation of each transit depth requires solving line-by-line radiative transfer in a transmission geometry in a plane-parallel atmosphere. Each terminator atmosphere has its own set of chemical compositions, P–T profile, and cloud/haze properties. Each model atmosphere has a pressure grid with a number of layers uniformly spaced in $\log_{10}(P)$, and a corresponding radial grid determined by hydrostatic

equilibrium. As with the 1D models described in Section 4, the calculation of hydrostatic equilibrium considers altitude-dependent gravity and an atmospheric mean molecular weight determined by the model's chemical composition.

The resulting two-dimensional model is given by

$$\Delta_{\lambda,2D} = \Phi_{T_1}\Delta_{\lambda,T_1} + \Phi_{T_2}\Delta_{\lambda,T_2}, \quad (8)$$

where Φ_{T_i} is the fraction of the total planetary atmosphere that terminator T_i represents. The sum of the terminator fractions follows the unit-sum constraint. For the case of a homogeneous atmosphere, the total fraction of one of the terminators becomes unity and we recover the transit depth for a homogeneous 1D planet atmosphere (e.g., Welbanks & Madhusudhan 2021).

6.2. 2D Retrieval Setup

The atmospheric retrieval setup follows the description in Section 4.2 for the parameter estimation scheme, number of nested sampling live points, sources of opacity, and number of pressure layers. Although the prescription in Section 6.1 can incorporate the effects of inhomogeneous clouds and hazes in each terminator, we limit our models to clear atmospheres only, to focus on the effects of compositional and thermal inhomogeneities. Future work will explore the effects of including inhomogeneous clouds and hazes in these models. Additionally, we do not retrieve the terminator fraction for each model; instead, we assume that each $\Phi_{T_i} = 0.5$. Due to the symmetry of the problem, the retrieved posterior distributions for the parameters of each terminator are commutable and representative of either.

We explore the three cases considered in Section 4 of the warm, hot, and ultra-hot Jupiters. The priors for these models are the same as those used for the clear models in Section 4.2 shown in Table B1 in Appendix B. The models have a total of 21 parameters for the warm Jupiter and ultra-hot Jupiter cases (eight chemical abundances, 12 *P–T* parameters, and one parameter for R_p at $P_{ref} = 10$ bar), and 23 parameters for the hot Jupiter case (10 chemical abundances, 12 *P–T* parameters, and one parameter for R_p at $P_{ref} = 10$ bar).

6.3. 2D Retrieval Results

Figure 8 shows the results of our 2D retrieval on the synthetic observations of a planet with asymmetric evening and morning terminators. The top row of Figure 8 shows the retrieved 2D spectrum, the middle row shows the 2D *P–T* profile, and the bottom row shows the average of the morning and evening abundances. In Appendix D, we show the retrieved spectra, *P–T* profiles, and abundances for each morning and evening terminator.

For all three cases, the retrieved 2D transmission spectrum is in good agreement with the synthetic observations. Furthermore, the retrieved spectra for each of the terminators (e.g., top row in Figures D1, D2, and D3) are consistent with the input morning and evening spectra used in the linear combination. While the retrieved 2D transmission spectra provide a fit to the observations, the retrieved 1D spectra for each terminator provides important information about the family of models contributing to the 2D spectra. Additionally, by inspecting the retrieved confidence contours of the morning and evening spectra, we can appreciate which wavelength ranges are affected by the inhomogeneities in the asymmetric terminators. For example, the retrieved transmission spectrum for each terminator in the hot Jupiter case seen in Figure D2 shows that the confidence intervals are wider in the HST-STIS wavelengths ($\lesssim$1 μm) where the TiO and VO abundance inhomogeneities have a strong impact, compared to the HST-WFC3 wavelengths ($\sim$1.1–1.8 μm) with strong contributions from a homogeneous H_2O abundance.

The retrieved 2D *P–T* profiles in the photosphere for transmission spectra ($P \sim 10^{-3}$–10^{-1} bar) are all consistent with the average of the morning and evening terminator temperatures. The retrieved *P–T* profiles for each terminator have wide 1σ and 2σ confidence contours consistent with the input *P–T* profiles (e.g., middle row in Figures D1, D2, and D3). Overall, the use of this 2D retrieval results in no significant biases in the thermal inferences at the photosphere for these input models with asymmetric terminators.

Similarly, the average retrieved chemical abundances are consistent with the average of the input abundances within $\sim 1\sigma$ for all atmospheric cases. The retrieved constraints on the average chemical abundances are comparable to those obtained with existing observations and models with inhomogeneous clouds and hazes ($\lesssim$1 dex; see, e.g., Welbanks et al. 2019). Furthermore, the posterior distributions for the retrieved chemical abundances of each terminator (e.g., bottom row in Figures D1, D2, and D3) are consistent with the input values within $\sim 1\sigma$. The posterior distributions for the chemical species with strong inhomogeneities (e.g., present in one terminator and absent in the other) are multimodal and suggestive of their presence in one terminator and absence in the other.

Finally, we compare these 2D models with the 1D models explored in Section 4. We find that, for the synthetic observations employed, there is no significant preference for the 2D models over the 1D models in the warm and hot Jupiter scenarios. However, our 2D model is preferred over all 1D models at a $\gtrsim 4\sigma$ level for the ultra-hot Jupiter scenario. This suggests that our 2D atmospheric model is better than its 1D counterparts at explaining the spectroscopic features of asymmetric terminators, especially those with strong chemical and thermal inhomogeneities, as expected.

In summary, the implementation of a 2D retrieval results in no distinguishable biases in the inferred *P–T* profile, atmospheric chemical composition, or transmission spectra for the atmospheric cases investigated. Additionally, this 1D+1D procedure provides us with meaningful inferences that show the families of atmospheric models that can explain the observed spectra, as well as the individual properties of each terminator. This new atmospheric model enables initial inferences about chemical and thermal inhomogeneities in exoplanet atmospheres, and it is ready to be applied to current and upcoming ground and space-based observations.

7. Summary and Discussion

We investigated the origin of previous inferences of thermal anomalies in 1D retrievals of transmission spectra. We revisited results from homogeneous retrieval studies of a large sample of exoplanets and informed their thermal expectations using GCM studies. Then, we derived expectations for an equivalent 1D temperature from a 2D spectrum using a semi-analytic formalism and confirmed them with atmospheric retrievals. Additionally, we perform 1D atmospheric retrievals on synthetic observations of a 2D spectrum with asymmetric terminators and on existing observations of the hot Jupiter

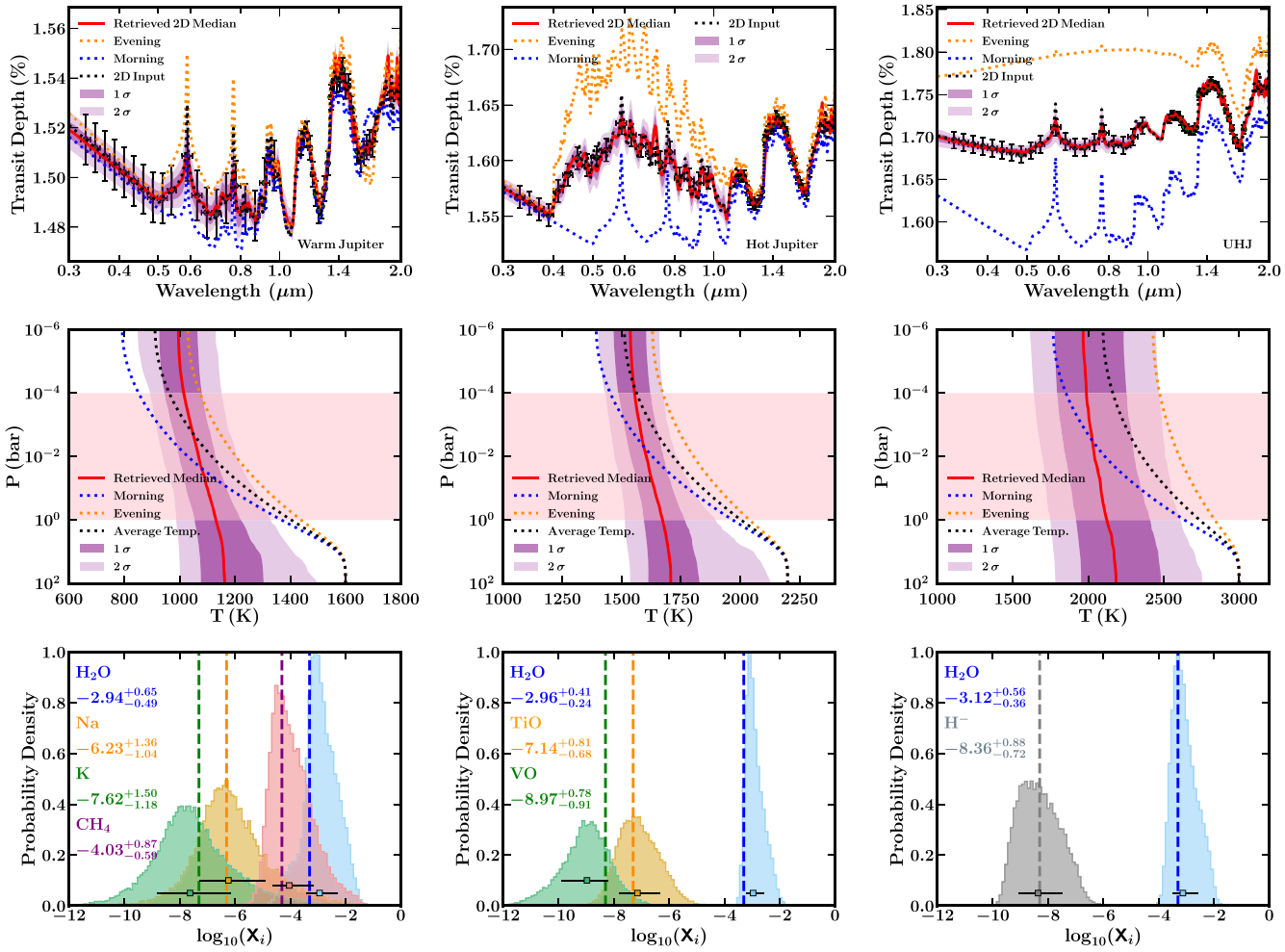

Figure 8. Results from our 2D retrievals on synthetic data from a 2D model. Each column corresponds to an atmospheric case explained in Section 4 adopted after MGL20: a warm Jupiter ($\bar{T} \sim 1000$ K), a hot Jupiter ($\bar{T} \sim 1600$ K), and an ultra-hot Jupiter ($\bar{T} \sim 2200$ K). Top: A morning spectrum (blue) and an evening spectrum (orange) are linearly combined to produce a 2D model (black) in order to generate HST-STIS and HST-WFC3 synthetic observations (black error bars). The retrieved median 2D spectrum (red) and 1σ and 2σ confidence intervals (purple shaded regions) from the 2D retrieval are shown. Middle: The true morning (blue) and evening (orange) *P–T* profiles used to generate the 2D model and synthetic data, along with their average (black), are shown using dotted lines. The retrieved 2D *P–T* profile is shown using a red line (median) with purple shaded regions showing the 1σ and 2σ confidence intervals. Pink horizontal shaded region shows the estimated photospheric pressure range from MGL20. Bottom: Posterior distributions corresponding to the average of the morning and evening abundances, with error bars indicating the median and 1σ intervals (numerical value shown in the labels). The averages of the input morning and evening abundances are shown using vertical dashed lines.

WASP-43b and ultra-hot Jupiter WASP-103b. Finally, we introduce a multidimensional 2D atmospheric retrieval for planets with asymmetric terminators. Here, we summarize our conclusions regarding atmospheric temperature estimates from exoplanetary transmission spectra.

1. Existing atmospheric temperature estimates from the population study of Welbanks et al. (2019) are generally consistent with equilibrium and skin temperature expectations, and fall within the physically plausible range of the terminator photospheric temperature estimates from GCM studies.
2. Our semi-analytic derivation finds that the 1D equivalent temperature from a 2D spectrum with asymmetric terminators is the average of the temperatures of the morning and evening terminators. Our retrieval with semi-analytic models confirms this expectation. Furthermore, the 1D equivalent volume mixing ratio is not expected to be the average of the morning and evening abundances under the semi-analytic assumptions.
3. Our numerical retrievals using synthetic observations find that previous inferences of temperature biases were affected by their choice of *P–T* parameterization and resulted in temperatures estimates that were lower by a factor of two or more. On the other hand, models using well-validated *P–T* parameterizations result in no significant biases for warm and hot Jupiters, and comparatively smaller biases for the chosen ultra-hot Jupiter scenario.
4. Using synthetic data, we find that models with inhomogeneous clouds and hazes, which are inherently multidimensional, find chemical abundances consistent with expectations for most cases. Additionally, the retrieved posterior distributions for chemical species with strong abundance inhomogeneities between the morning and evening terminators can be multimodal, suggesting that the median retrieved abundance is not a reliable indicator of the overall abundance of the atmosphere.
5. Our reanalysis of published transmission spectra for the hot Jupiter WASP-43b and ultra-hot Jupiter WASP-103b

finds that previous inferences of low atmospheric temperatures are likely the result of model assumptions such as isothermal *P–T* profiles, and not due to limitations in 1D models due to asymmetric terminators. When these model assumptions are relaxed, our atmospheric models retrieve warmer atmospheric temperatures that are generally consistent with equilibrium temperature estimates, GCM studies, and phase-curve observations.
6. We introduce the first 2D atmospheric free retrieval for transiting exoplanets. This multidimensional scheme allows for the retrieval of the spectrum, thermal properties, and chemical abundances of asymmetric terminators. Furthermore, this framework helps identify the wavelength range most affected by the inhomogeneities among terminators. This multidimensional framework is ready to be confronted with the high-precision and broad wavelength observations expected from JWST.

Additionally, we find that a series of factors likely affected previous studies inferring anomalously cool temperatures in atmospheric retrievals of transmission spectra, starting with MGL20. These include:

1. Failing to consider the uncertainties in the retrieved temperature estimates from the literature.
2. Using the retrieved temperature at the top of the atmosphere (10^{-6} bar) as a representative temperature for the photosphere in transmission spectra.
3. Assuming that the temperatures probed with transmission spectroscopy cannot be cooler than the skin temperature for a gray atmosphere.
4. Choosing inappropriate *P–T* profile parameterizations.
5. Generalizing findings derived from non-cloudy models and extreme atmospheric scenarios that may not be representative of the general population of exoplanets.
6. Assuming that the atmospheric properties at the terminator can be inferred from a single transit depth measurement at an arbitrary wavelength.

We shall next discuss additional considerations for future works as we move toward the characterization of transiting exoplanets with multidimensional models.

7.1. Understanding the Statistical Nature of Retrievals

Our study highlights the importance of interpreting the inferred atmospheric properties as statistical estimates with associated uncertainties. After all, the products of an atmospheric retrieval are the posterior distributions of the model parameters given the assumptions of the model. We emphasize the importance of interpreting the retrieved median results in the context of the posterior distribution they come from. As explained above, if the posterior distribution is multimodal, the median value may not be representative of the overall parameter recovered. Additionally, choosing the most probable mode and ignoring others can skew the interpretation of the results. Similarly, it is important to consider the 1σ and 2σ confidence intervals in the retrieved *P–T* profiles, especially for transmission spectroscopy where temperature constraints can have precisions of a few 100 K at the photosphere.

For example, MGL20 compute transmission spectra for the hot Jupiter WASP-17b and the ultra-hot Jupiter WASP-12b using self-consistent atmospheric profiles, and retrieve them using 1D models. Their retrieval results are consistent with the input models for WASP-17b. However, the retrieved solutions for WASP-12b, which are multimodal in nature, are interpreted as inconsistent and biased. Their interpretation focuses on the most probable mode and does not explore the properties of the other modes. Indeed, their subdominant mode is consistent with the input parameters and is indicative of the true input answer. Similarly, their suggested biases in the retrieved photospheric temperatures for the same models may be less severe when considering that the retrieved 1σ and 2σ confidence intervals shown in their Figure 4 are largely consistent with the input profiles, especially near the slant photosphere.

Next, there is the consideration of observations using white noise (i.e., independently distributed Gaussian errors). For instance, Feng et al. (2018) highlight the possibility of biases in retrieved properties due to different noise instances. This argument is the motivation for MGL20 to ignore a Gaussian scatter in their synthetic transit depths. However, the likelihood function in the retrieval framework employed in their study assumes that the observations have independently distributed Gaussian errors (MacDonald & Madhusudhan 2017). As a result, utilizing observations that do not have independently distributed Gaussian errors invalidates the assumption in their likelihood function. Future work may look into the effects of invalidating the likelihood function and how it affects the retrieved inferences and their uncertainties.

Finally, it is important to highlight that any atmospheric inference is only as good as the assumptions of the models employed. For example, clear atmospheric models can result in more precise abundance estimates than models with inhomogeneous clouds and hazes (e.g., Welbanks & Madhusudhan 2019). Failing to consider the limitations of these seemingly more precise models—and extrapolating the lessons learned from them to models with *different* model assumptions—would be erroneous. As such, it is important to contextualize the inferences made by studies using simplified models by their limiting assumptions, and to avoid generalizing their conclusions to a broader family of models.

As we move toward the characterization of exoplanet atmospheres with multidimensional models, an investigation of the model and data limitations will be paramount. Future studies will be able to investigate the uncertainties in the retrieved atmospheric properties as a function of model complexity. Moreover, future studies will also be able to investigate the degeneracies introduced by building these multidimensional frameworks. Overall, it will be important to keep in mind the statistical nature of retrievals and their output as we inform inferences made with current and upcoming facilities.

7.2. Obtaining Temperature Constraints from Transmission Spectroscopy

Finally, we note that the constraints obtained for the *P–T* profiles in this work and in the literature (see, e.g., Table 1), are of the order of a few 100 K in precision. This is largely due to the fact that transmission spectroscopy is limited in constraining the vertical temperature structure of the planet, as the main temperature dependence of the spectrum is encoded through the scale height and not directly through thermal emission. Nevertheless, these temperature constraints are still important to obtain information about the nominal conditions at the terminator, and they are the only means of doing so for planets

that may not be conducive for emission spectroscopy. But where possible, better constraints on the atmospheric temperature structure can be obtained through thermal emission spectra and phase curves. For instance, emission spectroscopy encodes in its observed spectrum the brightness temperature of the planet at different wavelengths, allowing for robust constraints on the *P–T* profile in the atmosphere (see, e.g., Madhusudhan 2019).

7.3. Concluding Remarks

Our study highlights the importance of considering the statistical nature of retrievals and contextualizing any atmospheric inferences by the model assumptions inevitably employed in deriving them. As we incorporate previously overlooked physical considerations, we must systematically explore the limitations of our models and the impact of their assumptions on the inferred atmospheric properties and their uncertainties. We caution against encompassing all possible biases in 1D retrievals under the scope of inhomogeneous terminators/hemispheres without considering the impact of chemical equilibrium assumptions, simplified semi-analytic models and isothermal atmospheres (e.g., Welbanks & Madhusudhan 2019), inhomogeneities in the presence of clouds and hazes (e.g., Line & Parmentier 2016; Barstow 2020; Welbanks & Madhusudhan 2021), and other model considerations such as the choice of *P–T* parameterization (e.g., Blecic et al. 2017). By jointly considering the limitations of our data and models, we can provide robust and reliable atmospheric inferences.

The future of transmission spectroscopy is bright. For current observations, our results suggest that state-of-the-art 1D models are overall unaffected by terminators with compositional and thermal inhomogeneities in most cases. Only the most extreme terminator asymmetries result in biases for 1D models assuming homogeneous conditions, as expected. For these exotic cases, we have extended our models and relaxed the assumption of symmetric planet terminators. These 2D models successfully capture the average atmospheric properties of these planets, and provide an insightful window into the individual properties of each terminator. Not only does this more advanced framework provide a fit to the observed spectra, it also reveals the wavelength ranges most affected by planetary inhomogeneities. Interpreting upcoming ground- and space-based observations, including those with JWST, using our new multidimensional retrieval framework promises to unveil a new dimension for understanding exoplanet atmospheres.

L.W. thanks the Gates Cambridge Trust for support toward his doctoral studies. Support for this work was provided by NASA through the NASA Hubble Fellowship grant #HST-HF2-51496.001-A awarded by the Space Telescope Science Institute, which is operated by the Association of Universities for Research in Astronomy, Inc., for NASA, under contract NAS5-26555. This work was performed using resources provided by the Cambridge Service for Data Driven Discovery (CSD3) operated by the University of Cambridge Research Computing Service (www.csd3.cam.ac.uk), provided by Dell EMC and Intel using Tier-2 funding from the Engineering and Physical Sciences Research Council (capital grant EP/P020259/1), and DiRAC funding from the Science and Technology Facilities Council (www.dirac.ac.uk). L.W. thanks Siddharth Gandhi for insightful conversations regarding the H^- opacity used in this work. L.W. thanks Savvas Constantinou, Michael Zhang, Vivien Parmentier, and Michael Line for fruitful conversations regarding semi-analytic models of transmission spectra.

Appendix A
Temperature and Mixing Ratio Equivalence between a 1D and a 2D Model

Here, we derive thermal and chemical expectations from equating a 2D transmission spectrum, resulting from the linear combination of two 1D transmission spectra, to a 1D spectrum. For this, we use semi-analytic models of transmission spectra that assume isobaric and isothermal atmospheres. While these models have simplified and often unphysical assumptions, their analytic tractability makes them useful tools to help build initial intuition about some of the atmospheric properties. The 1D transmission spectrum under the assumptions of an isobaric, isothermal atmosphere, a single chemical absorber, hydrostatic equilibrium, and ideal gas law is given by (e.g., Lecavelier Des Etangs et al. 2008a, 2008b; de Wit & Seager 2013; Bétrémieux & Swain 2017; Heng & Kitzmann 2017; Sing 2018)

$$\Delta_{\lambda,1D} = \frac{R_{p\,1D}^2 + 2R_{p\,1D}H_{1D}(\gamma + \ln\tau_{1D})}{R_{star}^2}, \tag{A1}$$

where $H_{1D} = kT_{1D}(\mu g)^{-1}$ is the 1D scale height, $R_{p\,1D}$ is the reference radius at a reference pressure P_0, γ is the Euler–Mascheroni constant, and τ_{1D} is the wavelength-dependent optical depth at the reference planetary radius and reference pressure

$$\tau_{1D} = \frac{P_0}{kT_{1D}}\sqrt{2\pi R_{p\,1D}H_{1D}}X_{1D}\,\sigma_\lambda(T_{1D}), \tag{A2}$$

assuming a single absorber with abundance X_{1D} and isobaric, temperature-dependent cross section $\sigma_\lambda(T_{1D})$.

Next, let the 2D transmission spectra be the result of a linear combination of two 1D spectra, each corresponding to a planetary terminator, M for morning and E for evening:

$$\Delta_{\lambda,2D} = \frac{\Delta_{\lambda,M} + \Delta_{\lambda,E}}{2}. \tag{A3}$$

The 1D spectrum for each terminator is given by Equation (A1), where instead of the 1D parameters (i.e., H_{1D}, $R_{p\,1D}$, and τ_{1D}), we use the parameters for each of the terminators (i.e., H_E, H_M, τ_E, and τ_M) and a reference radius $R_{p\,2D}$:

$$\Delta_{\lambda,2D} = \frac{R_{p\,2D}^2 + R_{p\,2D}H_M(\gamma + \ln\tau_M) + R_{p\,2D}H_E(\gamma + \ln\tau_E)}{R_{star}^2}. \tag{A4}$$

Our objective is to find the relationship between the atmospheric properties (temperature and abundance) of the 1D model and those of the evening and morning terminators in the 2D models.

We begin by requiring that the 1D model correctly reproduces the transmission spectrum of the 2D model. We assume that the shape of the spectral features in transit transmission spectra encode the information about the exoplanetary atmospheric properties, as shown by Lecavelier

Des Etangs et al. (2008a), Benneke & Seager (2012), and Line & Parmentier (2016). We equate the shape of the spectral features resulting from both models by considering the difference between transit depths at two wavelengths λ_1 and λ_2 for each model. The difference in transit depth for the 1D model in Equation (A1) is then

$$\delta\Delta_{\lambda_{2-1},1D} = \Delta_{\lambda_2,1D} - \Delta_{\lambda_1,1D} = 2\frac{R_{p\,1D}}{R_{star}^2}H_{1D}\ln\left(\frac{\sigma_{\lambda_2}(T_{1D})}{\sigma_{\lambda_1}(T_{1D})}\right). \quad (A5)$$

This dependence of the relative transit depth on the cross sections is well-known (e.g., Sing 2018), and is equivalent to the definition of spectral shape in Equation (5) of Line & Parmentier (2016). The corresponding result for the 2D model in Equation (A4) is

$$\delta\Delta_{\lambda_{2-1},2D} = \Delta_{\lambda_2,2D} - \Delta_{\lambda_1,2D} = \frac{R_{p\,2D}}{R_{star}^2}\left[H_M\ln\left(\frac{\sigma_{\lambda_2}(T_M)}{\sigma_{\lambda_1}(T_M)}\right) + H_E\ln\left(\frac{\sigma_{\lambda_2}(T_E)}{\sigma_{\lambda_1}(T_E)}\right)\right]. \quad (A6)$$

Equating (A5) and (A6) leads to

$$\frac{R_{p\,2D}}{R_{star}^2}\left[H_M\ln\left(\frac{\sigma_{\lambda_2}(T_M)}{\sigma_{\lambda_1}(T_M)}\right) + H_E\ln\left(\frac{\sigma_{\lambda_2}(T_E)}{\sigma_{\lambda_1}(T_E)}\right)\right] = 2\frac{R_{p\,1D}}{R_{star}^2}H_{1D}\ln\left(\frac{\sigma_{\lambda_2}(T_{1D})}{\sigma_{\lambda_1}(T_{1D})}\right). \quad (A7)$$

Following MGL20, we consider the case where the reference pressure is deep enough that it corresponds to a high optical depth and the reference radii are the same (i.e., $R_{p\,2D} = R_{p\,1D}$). This leads to

$$H_M\ln\left(\frac{\sigma_{\lambda_2}(T_M)}{\sigma_{\lambda_1}(T_M)}\right) + H_E\ln\left(\frac{\sigma_{\lambda_2}(T_E)}{\sigma_{\lambda_1}(T_E)}\right) = 2H_{1D}\ln\left(\frac{\sigma_{\lambda_2}(T_{1D})}{\sigma_{\lambda_1}(T_{1D})}\right). \quad (A8)$$

If the cross sections are allowed to vary weakly with T $\left(\text{i.e., } \frac{\sigma_{\lambda_2}(T_{1D})}{\sigma_{\lambda_1}(T_{1D})} \approx \frac{\sigma_{\lambda_2}(T_E)}{\sigma_{\lambda_1}(T_E)} \approx \frac{\sigma_{\lambda_2}(T_M)}{\sigma_{\lambda_1}(T_M)}\right)$, as in MGL20, we find

$$H_{1D} = \frac{H_E + H_M}{2}. \quad (A9)$$

Finally, under the assumptions of constant gravity and constant mean molecular weight that are part of this semi-analytic treatment by construction, Equation (A9) readily implies that

$$T_{1D} = \frac{T_E + T_M}{2}, \quad (A10)$$

i.e., the isothermal temperature derived using the equivalent 1D model is the average of the two isotherms in the 2D model.

We next assess the chemical abundances in the 1D model. We begin by equating the 1D transit depth to the 2D transit depth, i.e., $\Delta_{\lambda,2D} = \Delta_{\lambda,1D}$:

$$\frac{R_{p\,1D}^2 + 2R_{p\,1D}H_{1D}(\gamma + \ln\tau_{1D})}{R_{star}^2} = \frac{R_{p\,2D}^2 + R_{p\,2D}H_M(\gamma + \ln\tau_M) + R_{p\,2D}H_E(\gamma + \ln\tau_E)}{R_{star}^2}. \quad (A11)$$

Assuming $R_{p\,2D} = R_{p\,1D}$, as above, and rearranging the terms leads to

$$\gamma(2H_{1D} - H_E - H_M) = H_M\ln\tau_M + H_E\ln\tau_E - 2H_{1D}\ln\tau_{1D}. \quad (A12)$$

Equation (A9) implies that the left-hand side of Equation (A12) is zero. As a result,

$$\ln\tau_{1D} = \frac{H_M}{H_E + H_M}\ln\tau_M + \frac{H_E}{H_E + H_M}\ln\tau_E. \quad (A13)$$

Again, under the assumptions of this semi-analytic treatment, the gravity and mean molecular weight are constants; this further simplifies the expression to

$$\ln\tau_{1D} = \frac{T_M}{T_E + T_M}\ln\tau_M + \frac{T_E}{T_E + T_M}\ln\tau_E, \quad (A14)$$

Next, we rearrange Equation (A14) and use the definition of the optical depth in Equation (A2) to obtain

$$\frac{P_{0,1D}}{kT_{1D}}\sqrt{2\pi R_{p\,1D}H_{1D}}X_{1D}\,\sigma_{1D} = \left(\frac{P_{0,M}}{kT_M}\sqrt{2\pi R_{p\,2D}H_M}X_M\,\sigma_M\right)^{\frac{T_M}{T_E+T_M}} \times \left(\frac{P_{0,E}}{kT_E}\sqrt{2\pi R_{p\,2D}H_E}X_E\,\sigma_E\right)^{\frac{T_E}{T_E+T_M}}, \quad (A15)$$

where we have expressed the wavelength-dependent cross sections evaluated at the corresponding temperature $\sigma_\lambda(T_i) = \sigma_i$ for simplicity. Substituting our result from Equation (A10) and assuming $R_{p\,1D} = R_{p\,2D}$ gives

$$P_{0,1D}\,X_{1D}\,\sigma_{1D} = \sqrt{\frac{T_E + T_M}{2}}\,(P_{0,M}\,X_M\,\sigma_M)^{\frac{T_M}{T_E+T_M}} \times (P_{0,E}\,X_E\,\sigma_E)^{\frac{T_E}{T_E+T_M}} \times T_M^{-\frac{T_M}{2(T_E+T_M)}}T_E^{-\frac{T_E}{2(T_E+T_M)}}, \quad (A16)$$

which is the expression that represents the 1D atmospheric properties (i.e., reference pressure, single absorber abundance, and cross section) as a function of the properties of the morning and evening terminators.

We can further recast Equation (A16), following MGL20, in terms of the average temperature of the terminator $\bar{T} = \frac{T_E + T_M}{2}$ and the deviation $\Delta T = \frac{T_E - T_M}{2}$, i.e., $T_E = \bar{T} + \Delta T$ and $T_M = \bar{T} - \Delta T$. We can also define

$$\alpha = \frac{T_E}{\bar{T}} = 1 + \frac{\Delta T}{\bar{T}}, \quad \beta = \frac{T_M}{\bar{T}} = 1 - \frac{\Delta T}{\bar{T}}. \quad (A17)$$

Using these quantities, we find

$$P_{0,1D}\, X_{1D}\, \sigma_{\bar{T}} = \bar{T}^{\frac{1}{2}}(P_{0,M}\, X_M\, \sigma_M)^{\frac{\beta}{2}}(P_{0,E}\, X_E\, \sigma_E)^{\frac{\alpha}{2}} \times (\bar{T} - \Delta T)^{-\frac{\beta}{4}}(\bar{T} + \Delta T)^{-\frac{\alpha}{4}}. \quad \text{(A18)}$$

A.1. Interpreting the Semi-analytic Result

First, Equation (A18) shows that, under the assumptions of this semi-analytic treatment, the 1D chemical abundance is not the algebraic average of the abundances of the morning and evening terminators. Second, Equation (A18) shows the well-known degeneracy between the reference pressure and abundance that results from this semi-analytic treatment (see, e.g., Lecavelier Des Etangs et al. 2008a; Heng & Kitzmann 2017; Welbanks & Madhusudhan 2019). If the wavelength dependence of the cross section is known, this result suggests that one needs to assume an abundance to derive the reference pressure, or assume a reference pressure to derive an abundance (e.g., Lecavelier Des Etangs et al. 2008a). Therefore, without any assumptions about the reference pressure of the 1D model atmosphere, the transit depth at a single wavelength cannot provide enough information to obtain a single 1D chemical abundance under this semi-analytic treatment.

As an illustration, let us consider the atmospheric scenario that serves as input conditions for Section 3.2. Let there be a hot Jupiter with a hot evening terminator of temperature $T_E = 2000$ K, H_2O abundance of $\log_{10}(X_{H_2O,E}) = -6.0$, and a reference pressure of $P_{0,E} = 10$ bar. The cooler morning terminator has a $T_M = 1000$ K and H_2O abundance of $\log_{10}(X_{H_2O,M}) = -3.0$. In order to derive the reference pressure for the morning terminator, we assume that the reference point in both terminators corresponds to the same reference radius and optical depth surface. We can use this assumption and Equation (A2) to derive an expression for the reference pressure of the morning terminator

$$P_{0,M} = P_{0,E}\frac{X_{H_2O,E}}{X_{H_2O,M}}\frac{\sigma_E}{\sigma_M}\sqrt{\frac{T_M}{T_E}}. \quad \text{(A19)}$$

If we assume, for simplicity, cross sections with small temperature variations (i.e., $\sigma_{1500} \approx \sigma_{1000} \approx \sigma_{2000}$) we find $P_{0,M} \approx 7$ mbar. Using the above input values, we obtain $\Delta T/\bar{T} = 1/3$, $\alpha = 4/3$, and $\beta = 2/3$.

Substituting the above values into Equation (A18) shows that, for any chosen value of X_{1D}, one can choose a different value of $P_{0,1D}$ to satisfy the equality. Indeed, in Section 3.2 we perform a retrieval on a synthetic 2D spectrum with the above inputs using a 1D semi-analytic model, and we find the expected degeneracy between the abundance and the reference pressure.

If, on the other hand, we assume a value for the reference pressure of the 1D model, we can derive a 1D abundance. We can choose an arbitrary pressure of $P_{0,1D} = 0.1$ bar for illustration. Then, $X_{1D} = 10^{-4}$. In Section 3.2, we perform a second semi-analytic retrieval on the same synthetic data, but this time we assume a reference pressure of 0.1 bar in the 1D model. This retrieval finds a 1D abundance consistent with the expected value of $\log_{10}(X_{H_2O}) = -4$.

A.2. Analytic Comparison with MGL20

The derivation in MGL20 considers the equivalent transit depth between a 1D and a 2D model at a single wavelength. This approach assumes that the atmospheric properties can be deduced from a transit depth measurement at a single wavelength, which is not feasible. Inference of atmospheric properties in transmission geometry requires measurements of the transit depth at two or more wavelengths, i.e., a transmission spectrum (Lecavelier Des Etangs et al. 2008a; Benneke & Seager 2012; Line & Parmentier 2016). Therefore, our derivation shown in Appendix A uses the spectral shape of the transmission spectrum, i.e., the transit depth at two or more wavelengths, to find the equivalent atmospheric properties between a 1D and a 2D model.

Implementing our procedure on the derivation of MGL20 results in the same outcome as the derivation shown in this work. This can be demonstrated by starting with Equation (A22) of MGL20, which shows the transit depth equivalence condition, and differentiating it with respect to λ in order to obtain the equivalence of the spectral shape between the two models. Following the assumptions in MGL20 that the reference pressure is deep enough that it corresponds to a high optical depth and that the reference radii are the same (i.e., $R_{p\,1D} = R_{p\,2D}$) leads to

$$H_{1D}\left(\frac{d\ln(\sigma_\lambda)}{d\lambda}\right) = \bar{H}\left(\frac{d\ln(\sigma_\lambda)}{d\lambda}\right), \quad \text{(A20)}$$

where $\bar{H} = \frac{H_E + H_M}{2}$ and σ_λ is the wavelength-dependent cross section assumed to vary weakly with temperature. Equation (A20) is equivalent to Equation (A8) and readily implies that $H_{1D} = \frac{H_E + H_M}{2}$ and $T_{1D} = \frac{T_E + T_M}{2}$.

Appendix B
Priors for Retrievals in This Work

The priors for the semi-analytic models in Section 3.2 are uniform for T_{1D} between 300 K and 3000 K, log-uniform for X_{H_2O} between 10^{-12} and $10^{-0.3}$, and log-uniform for P_{ref} between 10^{-2} bar and 10^{6} bar.

The priors adopted for the 1D models in Section 4 are shown in Table B1. The priors are mostly standardized, and they follow the description of MGL20 for the MGL20 models and those of Welbanks et al. (2019) and Welbanks & Madhusudhan (2021) for the clear and cloudy models. The prior for the temperature parameter at the top of the atmosphere (T_0) was chosen so that it could span the entire range of possible temperatures in a form analogous to that of the prior for T_{deep} chosen by MGL20. The priors for 2D models in Section 6 are the same as the clear atmosphere model column in Table B1.

Table B1
Parameters and Priors for Retrievals in This Work

Parameter	Prior Distribution	MGL20	Clear Atmosphere	Cloudy Atmosphere
X_i	Log-uniform	10^{-12}–$10^{-0.3}$	10^{-12}–$10^{-0.3}$	10^{-12}–$10^{-0.3}$
$T_{\rm deep}$	Uniform	400–3000 K	N/A	N/A
T_0	Uniform	N/A	400–4000 K	400–4000 K
$\alpha_{1,2}$	Uniform	0.02–2.00 $K^{-1/2}$	0.02–2.00 $K^{-1/2}$	0.02–2.00 $K^{-1/2}$
$P_{1,2,\rm cloud,ref}$	Log-uniform	10^{-6}–10^{2} bar	10^{-6}–10^{2} bar	10^{-6}–10^{2} bar
P_3	Log-uniform	10^{-2}–10^{2} bar	10^{-2}–10^{2} bar	10^{-2}–10^{2} bar
$R_{\rm p,10\ bar}$	Uniform	0.85–1.15 $R_{\rm p}$	N/A	N/A
$P_{\rm ref.}$	Log-uniform	N/A	10^{-6}–10^{2} bar	10^{-6}–10^{2} bar
a	Log-uniform	N/A	N/A	10^{-4}–10^{10}
γ	Uniform	N/A	N/A	−20–2
$\phi_{\rm clouds}$ $\phi_{\rm hazes}$ $\phi_{\rm clouds+hazes}$	Uniform	N/A	N/A	0–1

Note. N/A means that the parameter was not considered in the model by construction.

Appendix C
1D Retrievals with Synthetic Observations

Here, we present the retrieved transmission spectra and posterior distributions for the 1D retrievals in Section 4. Figure C1 shows the input transmission spectra (morning, evening, and their linear combination), the synthetic observations, and the retrieved median model and confidence intervals. Figure C2 shows the posterior distributions for the retrieved volume mixing ratios of the chemical species of interest for the warm Jupiter, hot Jupiter, and ultra-hot Jupiter atmospheric scenarios.

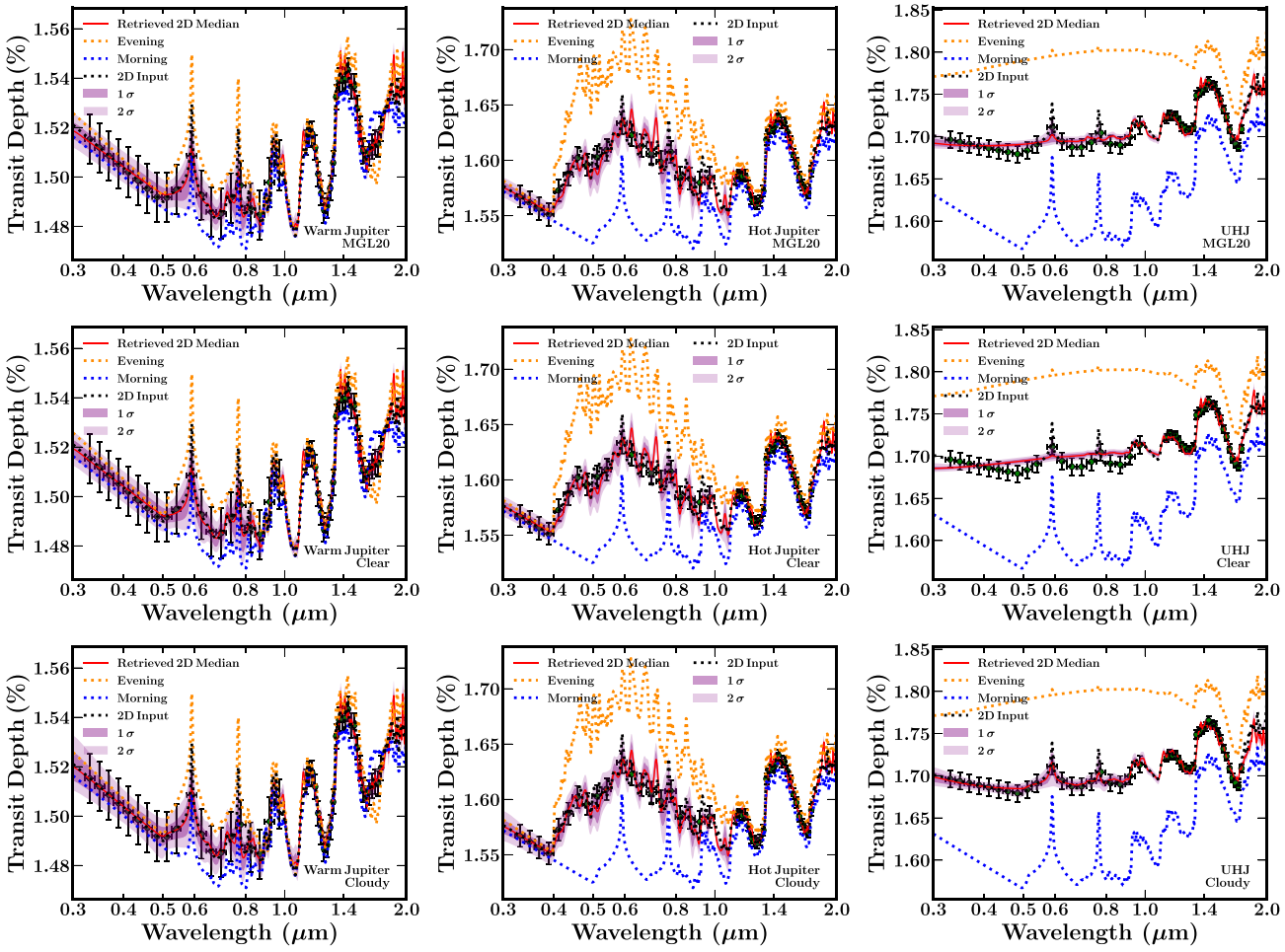

Figure C1. Retrieved transmission spectra for our numerical retrievals using 1D models on synthetic data from a 2D model in Section 4. Each column corresponds to an atmospheric case explained in Section 4 adopted after MGL20: a warm Jupiter ($\bar{T} \sim 1000$ K), a hot Jupiter ($\bar{T} \sim 1600$ K), and an ultra-hot Jupiter ($\bar{T} \sim 2200$ K). Each row corresponds to a different model strategy: a clear atmospheric model with the *P*–*T* parameterization from MGL20 (top), a cloud-free model with the *P*–*T* parameterization from Madhusudhan & Seager (2009; middle), and a model with inhomogeneous clouds and hazes from Welbanks & Madhusudhan (2021) and the *P*–*T* parameterization from Madhusudhan & Seager (2009; bottom). Each panel shows the morning (blue) and evening (orange) spectra that are linearly combined to produce a 2D model (black), along with HST-STIS/HST-WFC3 synthetic observations (error bars). The retrieved median spectrum (red) and 1σ and 2σ confidence intervals (purple shaded regions) from the 1D retrieval are shown.

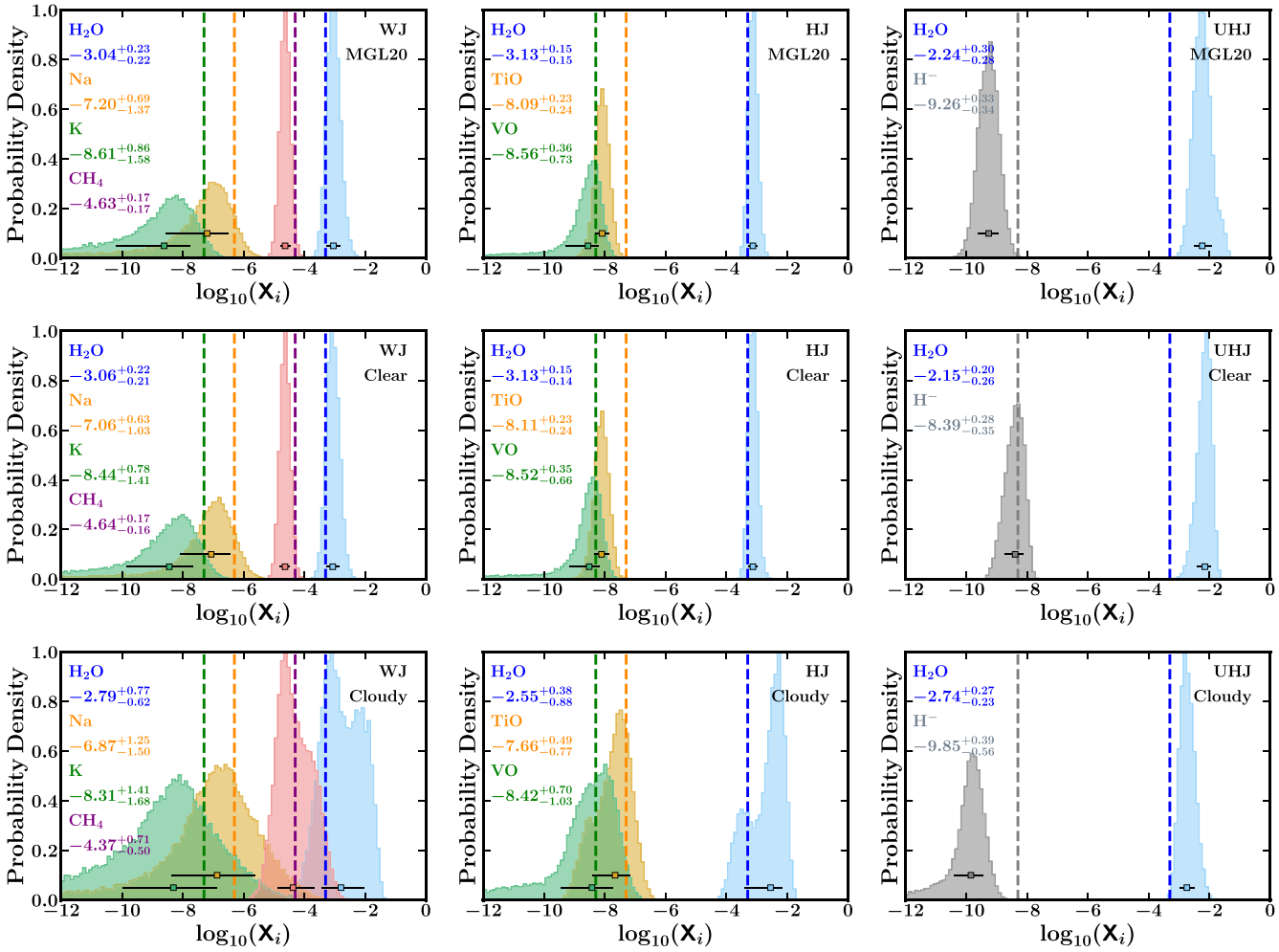

Figure C2. Retrieved posterior distributions for the chemical abundances in our numerical retrievals using 1D models on synthetic data from a 2D model in Section 4. Each column corresponds to an atmospheric case explained in Section 4 adopted after MGL20: a warm Jupiter ($\bar{T} \sim 1000$ K), a hot Jupiter ($\bar{T} \sim 1600$ K), and an ultra-hot Jupiter ($\bar{T} \sim 2200$ K). Each row corresponds to a different model strategy: a clear atmospheric model with the *P–T* parameterization from MGL20 (top), a cloud-free model with the *P–T* parameterization from Madhusudhan & Seager (2009; middle), and a model with inhomogeneous clouds and hazes from Welbanks & Madhusudhan (2021) and the *P–T* parameterization from Madhusudhan & Seager (2009; bottom). Each panel shows the retrieved mixing ratio posteriors and error bars indicating the median and 1σ intervals (numerical value shown in the labels). The averages of the morning and evening abundances are shown using vertical dashed lines.

Appendix D
2D Retrievals with Synthetic Observations

Here, we present the retrieved transmission spectra and posterior distributions for the 2D retrievals in Section 6. Figures D1, D2, and D3 show the retrieved spectra, *P–T* profiles, and chemical abundances for the morning and evening terminators. Additionally, the third column of each figure shows the retrieved 2D spectrum, 2D *P–T* profile, and average abundances as shown in Figure 8.

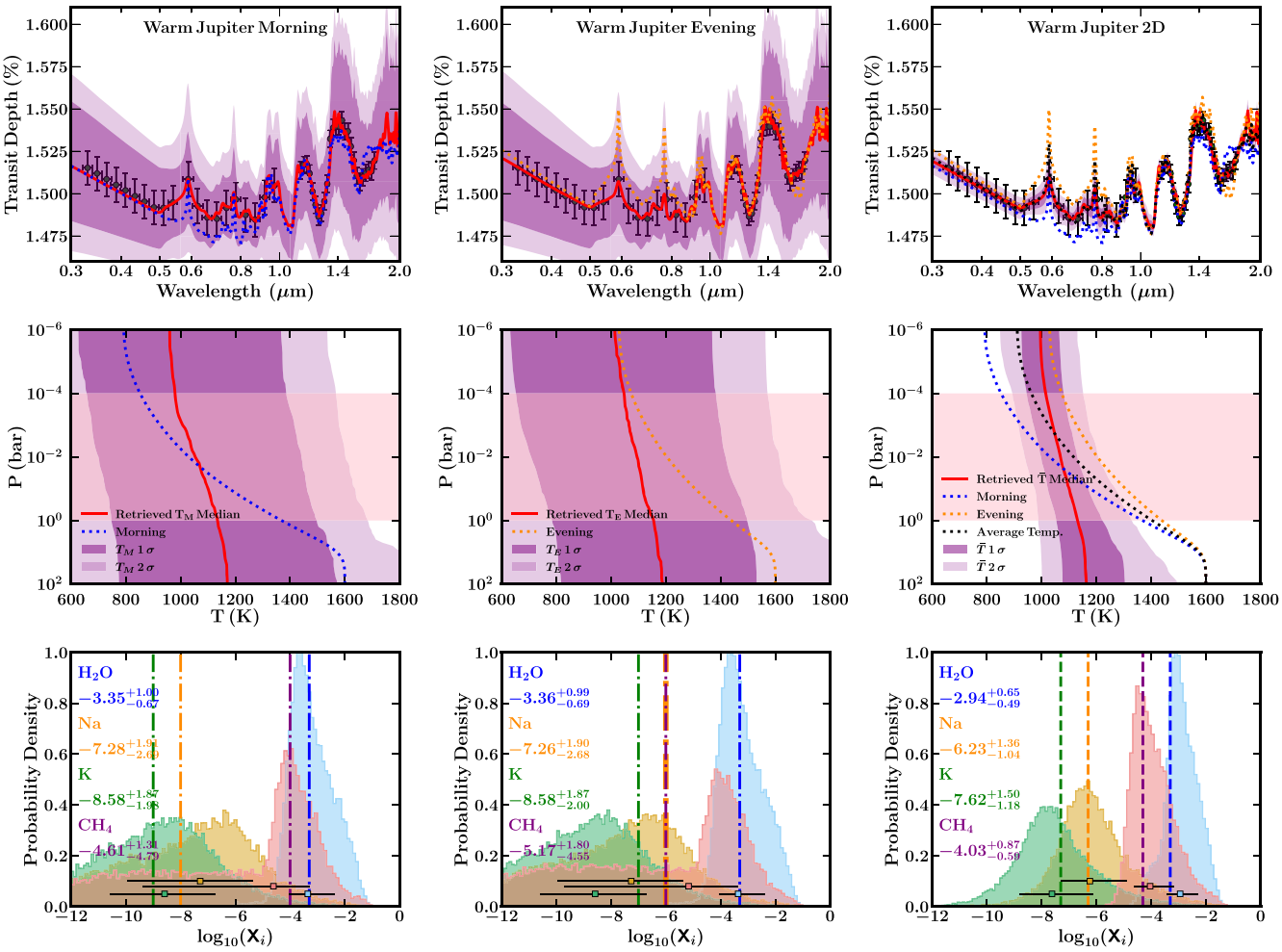

Figure D1. Results from our 2D retrievals on synthetic data from a 2D model for the warm Jupiter case. The top row shows the morning (blue) and evening (orange) spectra that are linearly combined to produce a 2D model (black) and HST-STIS/HST-WFC3 synthetic observations (error bars). The retrieved median spectrum (red) and 1σ and 2σ confidence intervals (purple shaded regions) from the retrieval are shown. Middle: The true morning (blue) and evening (orange) *P–T* profiles used to generate the 2D model and synthetic data, along with their average (black), are shown using dotted lines. The retrieved *P–T* profile is shown using a red line (median) with purple shaded regions showing the 1σ and 2σ confidence intervals. Pink horizontal shaded region shows the estimated photospheric pressure range from MGL20. Bottom: Posterior distributions corresponding to the chemical abundances and error bars indicating the median and 1σ intervals (numerical value shown in the labels). The colored dotted–dashed lines indicate the input values for each terminator, while the dashed lines show the average abundance of the morning and evening terminators. The left column shows the results for the morning terminator, the middle column shows the results for the evening terminator, and the right column shows the 2D results from the combination of the morning and evening terminators and the average abundances as in Figure 8.

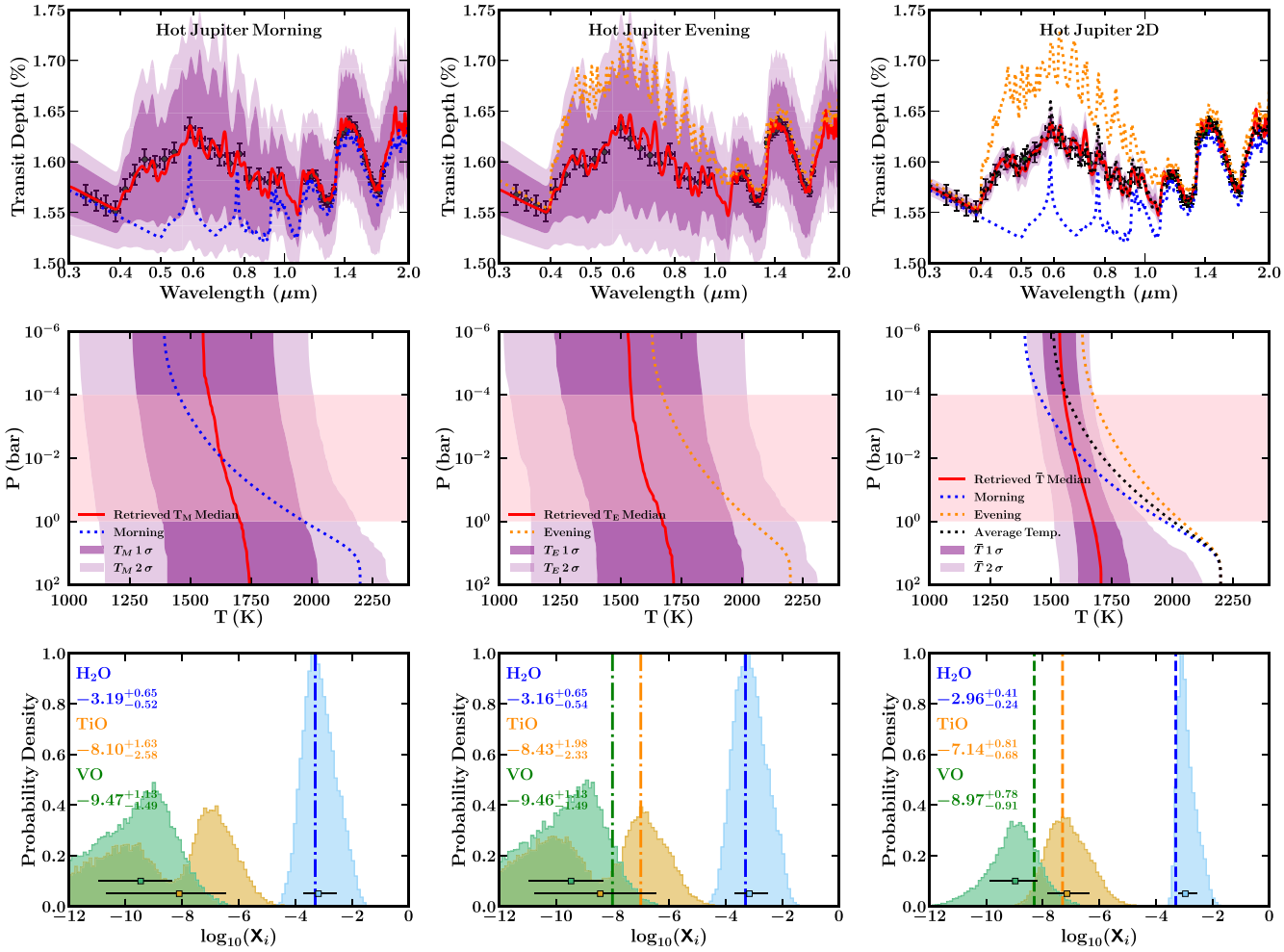

Figure D2. Same as Figure D1, but for the hot Jupiter case.

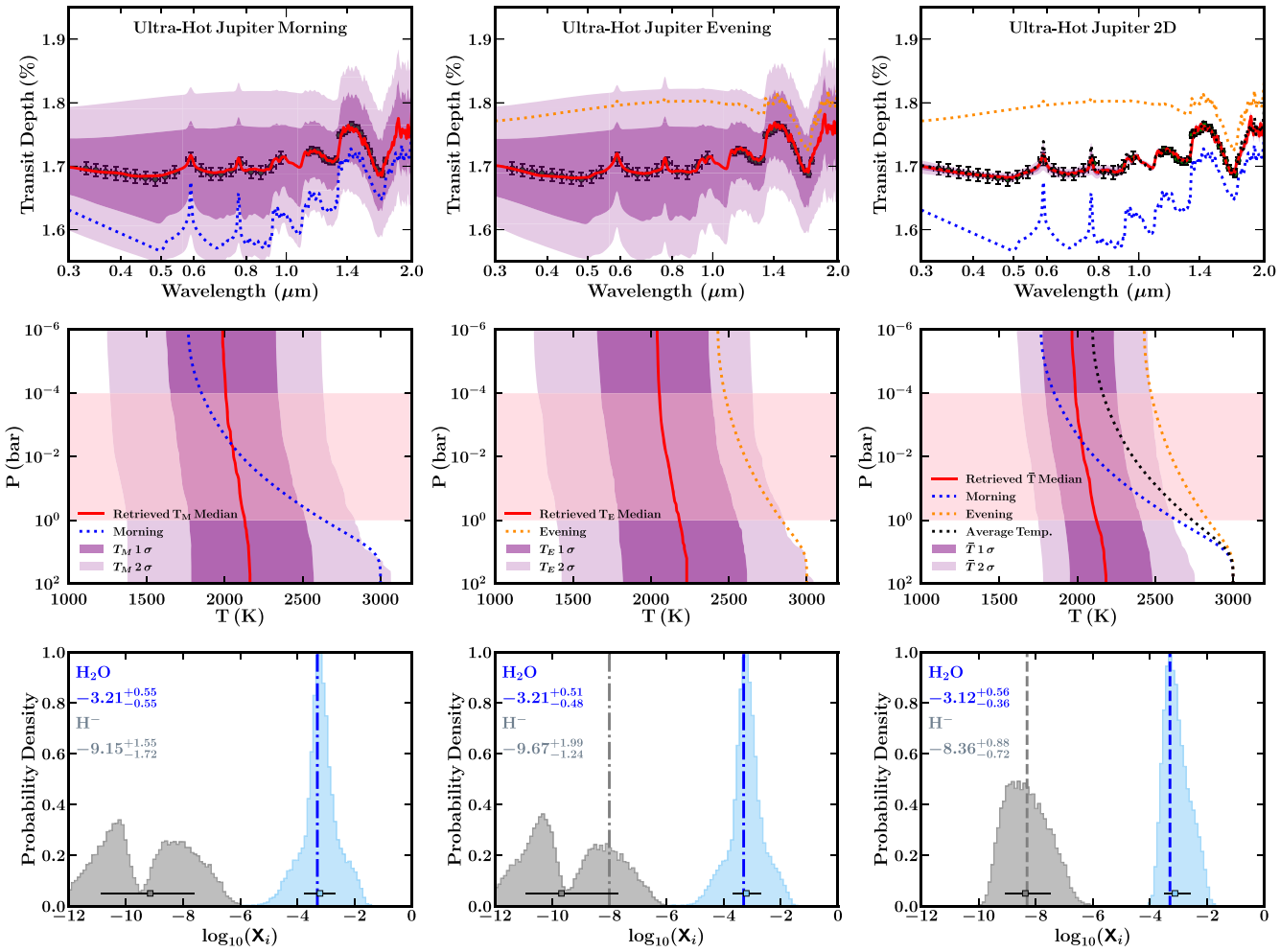

Figure D3. Same as Figure D1, but for the ultra-hot Jupiter case.

ORCID iDs

Luis Welbanks https://orcid.org/0000-0003-0156-4564
Nikku Madhusudhan https://orcid.org/0000-0002-4869-000X

References

Allard, N. F., Spiegelman, F., & Kielkopf, J. F. 2016, A&A, 589, A21
Allard, N. F., Spiegelman, F., Leininger, T., & Molliere, P. 2019, A&A, 628, A120
Arcangeli, J., Désert, J. M., Parmentier, V., Tsai, S. M., & Stevenson, K. B. 2021, A&A, 646, A94
Barber, R. J., Strange, J. K., Hill, C., et al. 2014, MNRAS, 437, 1828
Barstow, J. K. 2020, MNRAS, 497, 4183
Barstow, J. K., Aigrain, S., Irwin, P. G. J., & Sing, D. K. 2017, ApJ, 834, 50
Bauschlicher, C. W., Ram, R. S., Bernath, P. F., Parsons, C. G., & Galehouse, D. 2001, JChPh, 115, 1312
Benneke, B., Knutson, H. A., Lothringer, J., et al. 2019, NatAs, 3, 813
Benneke, B., & Seager, S. 2012, ApJ, 753, 100
Bétrémieux, Y., & Swain, M. R. 2017, MNRAS, 467, 2834
Blecic, J., Dobbs-Dixon, I., & Greene, T. 2017, ApJ, 848, 127
Brown, T. M. 2001, ApJ, 553, 1006
Brown, T. M., Charbonneau, D., Gilliland, R. L., Noyes, R. W., & Burrows, A. 2001, ApJ, 552, 699
Buchner, J., Georgakakis, A., Nandra, K., et al. 2014, A&A, 564, A125
Burrows, A., Rauscher, E., Spiegel, D. S., & Menou, K. 2010, ApJ, 719, 341
Caldas, A., Leconte, J., Selsis, F., et al. 2019, A&A, 623, A161
Charbonneau, D., Brown, T. M., Noyes, R. W., & Gilliland, R. L. 2002, ApJ, 568, 377
de Wit, J., & Seager, S. 2013, Sci, 342, 1473
Delrez, L., Madhusudhan, N., Lendl, M., et al. 2018, MNRAS, 474, 2334
Deming, D., Wilkins, A., McCullough, P., et al. 2013, ApJ, 774, 95
Dulick, M., Bauschlicher, C. W. J., Burrows, A., et al. 2003, ApJ, 594, 651
Espinoza, N., & Jones, K. 2021, AJ, 162, 165
Espinoza, N., Rackham, B. V., Jordán, A., et al. 2019, MNRAS, 482, 2065
Feng, Y. K., Line, M. R., Fortney, J. J., et al. 2016, ApJ, 829, 52
Feng, Y. K., Line, M. R., & Fortney, J. J. 2020, AJ, 160, 137
Feng, Y. K., Robinson, T. D., Fortney, J. J., et al. 2018, AJ, 155, 200
Feroz, F., Hobson, M. P., & Bridges, M. 2009, MNRAS, 398, 1601
Feroz, F., Hobson, M. P., Cameron, E., & Pettitt, A. N. 2019, OJAp, 2, 10
Fortney, J. J., Shabram, M., Showman, A. P., et al. 2010, ApJ, 709, 1396
Fortney, J. J., Sudarsky, D., Hubeny, I., et al. 2003, ApJ, 589, 615
Gandhi, S., & Madhusudhan, N. 2017, MNRAS, 472, 2334
Gandhi, S., & Madhusudhan, N. 2018, MNRAS, 474, 271
Gandhi, S., Madhusudhan, N., & Mandell, A. 2020a, AJ, 159, 232
Gandhi, S., Brogi, M., Yurchenko, S. N., et al. 2020b, MNRAS, 495, 224
Gillon, M., Anderson, D. R., Collier-Cameron, A., et al. 2014, A&A, 562, L3
Gillon, M., Triaud, A. H. M. J., Fortney, J. J., et al. 2012, A&A, 542, A4
Goyal, J. M., Mayne, N., Sing, D. K., et al. 2018, MNRAS, 474, 5158
Greene, T. P., Line, M. R., Montero, C., et al. 2016, ApJ, 817, 17
Hargreaves, R. J., Hinkle, K. H., Bauschlicher, C. W. J., et al. 2010, AJ, 140, 919
Hellier, C., Anderson, D. R., Collier Cameron, A., et al. 2011, A&A, 535, L7
Heng, K., & Kitzmann, D. 2017, MNRAS, 470, 2972
Hill, C., Yurchenko, S. N., & Tennyson, J. 2013, Icar, 226, 1673
Iro, N., Bézard, B., & Guillot, T. 2005, A&A, 436, 719
Iyer, A. R., & Line, M. R. 2020, ApJ, 889, 78
John, T. L. 1988, A&A, 193, 189
Kataria, T., Showman, A. P., Fortney, J. J., et al. 2015, ApJ, 801, 86
Kataria, T., Sing, D. K., Lewis, N. K., et al. 2016, ApJ, 821, 9
Kirk, J., Rackham, B. V., MacDonald, R. J., et al. 2021, AJ, 162, 34
Kreidberg, L., Bean, J. L., Désert, J.-M., et al. 2014a, Natur, 505, 69

Kreidberg, L., Bean, J. L., Désert, J.-M., et al. 2014b, ApJL, 793, L27
Kreidberg, L., Line, M. R., Parmentier, V., et al. 2018, AJ, 156, 17
Kurucz, R. L. 1992, RMxAA, 23, 45
Lacy, B. I., & Burrows, A. 2020, ApJ, 905, 131
Lecavelier Des Etangs, A., Pont, F., Vidal-Madjar, A., & Sing, D. 2008a, A&A, 481, L83
Lecavelier Des Etangs, A., Vidal-Madjar, A., Désert, J.-M., & Sing, D. 2008b, A&A, 485, 865
Lewis, N. K., Showman, A. P., Fortney, J. J., et al. 2010, ApJ, 720, 344
Lewis, N. K., Showman, A. P., Fortney, J. J., Knutson, H. A., & Marley, M. S. 2014, ApJ, 795, 150
Line, M. R., & Parmentier, V. 2016, ApJ, 820, 78
Line, M. R., Wolf, A. S., Zhang, X., et al. 2013, ApJ, 775, 137
MacDonald, R. J., Goyal, J. M., & Lewis, N. K. 2020, ApJL, 893, L43
MacDonald, R. J., & Madhusudhan, N. 2017, MNRAS, 469, 1979
Madhusudhan, N. 2018, in Handbook of Exoplanets, ed. H. J. Deeg & J. A. Belmonte (Berlin: Springer), 104
Madhusudhan, N. 2019, ARA&A, 57, 617
Madhusudhan, N., Crouzet, N., McCullough, P. R., Deming, D., & Hedges, C. 2014, ApJL, 791, L9
Madhusudhan, N., & Seager, S. 2009, ApJ, 707, 24
McKemmish, L. K., Yurchenko, S. N., & Tennyson, J. 2016, MNRAS, 463, 771
Mollière, P., Wardenier, J. P., van Boekel, R., et al. 2019, A&A, 627, A67
Moses, J. I., Line, M. R., Visscher, C., et al. 2013, ApJ, 777, 34
Moses, J. I., Visscher, C., Fortney, J. J., et al. 2011, ApJ, 737, 15
Nikolov, N., Sing, D. K., Fortney, J. J., et al. 2018, Natur, 557, 526
Parmentier, V., Fortney, J. J., Showman, A. P., Morley, C., & Marley, M. S. 2016, ApJ, 828, 22
Parmentier, V., & Guillot, T. 2014, A&A, 562, A133
Parmentier, V., Line, M. R., Bean, J. L., et al. 2018, A&A, 617, A110
Patrascu, A. T., Yurchenko, S. N., & Tennyson, J. 2015, MNRAS, 449, 3613
Pierrehumbert, R. T. 2010, Principles of Planetary Climate (Cambridge: Cambridge Univ. Press)
Pinhas, A., Madhusudhan, N., Gandhi, S., & MacDonald, R. 2019, MNRAS, 482, 1485
Pinhas, A., Rackham, B. V., Madhusudhan, N., & Apai, D. 2018, MNRAS, 480, 5314
Pluriel, W., Leconte, J., Parmentier, V., et al. 2022, A&A, 658, A42
Pluriel, W., Zingales, T., Leconte, J., & Parmentier, V. 2020, A&A, 636, A66
Pont, F., Knutson, H., Gilliland, R. L., Moutou, C., & Charbonneau, D. 2008, MNRAS, 385, 109
Rackham, B. V., Apai, D., & Giampapa, M. S. 2018, ApJ, 853, 122
Rackham, B. V., Apai, D., & Giampapa, M. S. 2019, AJ, 157, 96
Richard, C., Gordon, I. E., Rothman, L. S., et al. 2012, JQSRT, 113, 1276
Rothman, L. S., Gordon, I. E., Barber, R. J., et al. 2010, JQSRT, 111, 2139
Schwenke, D. W. 1998, FaDi, 109, 321
Seager, S. 2010, Exoplanet Atmospheres: Physical Processes (Princeton, NJ: Princeton Univ. Press)
Seager, S., & Sasselov, D. D. 1998, ApJL, 502, L157
Seager, S., & Sasselov, D. D. 2000, ApJ, 537, 916
Showman, A. P., Fortney, J. J., Lian, Y., et al. 2009, ApJ, 699, 564
Sing, D. K. 2018, in Astrophysics of Exoplanetary Atmospheres: 2nd Advanced School on Exoplanetary Science, ed. V. Bozza, L. Mancini, & A. Sozzetti (Berlin: Springer)
Sing, D. K., Fortney, J. J., Nikolov, N., et al. 2016, Natur, 529, 59
Steinrueck, M. E., Showman, A. P., Lavvas, P., et al. 2021, MNRAS, 504, 2783
Stevenson, K. B., Line, M. R., Bean, J. L., et al. 2017, AJ, 153, 68
Taylor, J., Parmentier, V., Irwin, P. G. J., et al. 2020, MNRAS, 493, 4342
Torres, G., Winn, J. N., & Holman, M. J. 2008, ApJ, 677, 1324
Venot, O., Hébrard, E., Agúndez, M., et al. 2012, A&A, 546, A43
Venot, O., Parmentier, V., Blecic, J., et al. 2020, ApJ, 890, 176
Weaver, I. C., López-Morales, M., Espinoza, N., et al. 2020, AJ, 159, 13
Welbanks, L., & Madhusudhan, N. 2019, AJ, 157, 206
Welbanks, L., & Madhusudhan, N. 2021, ApJ, 913, 114
Welbanks, L., Madhusudhan, N., Allard, N. F., et al. 2019, ApJL, 887, L20
Wende, S., Reiners, A., Seifahrt, A., & Bernath, P. F. 2010, A&A, 523, A58
Yurchenko, S. N., & Tennyson, J. 2014, MNRAS, 440, 1649
Yurchenko, S. N., Tennyson, J., Barber, R. J., & Thiel, W. 2013, JMoSp, 291, 69